EXPERIMENTAL EXAMINATION OF THE EFFECT OF OBSERVATION GEOMETRY ON LAND SURFACE TEMPERATURE ESTIMATES FROM REMOTELY SENSED GROUND BASED THERMAL IMAGERY

BY

TIMOTHY MICHAEL SLIWINSKI AND JACK A. PULEO

CENTER FOR APPLIED COASTAL RESEARCH

Ocean Engineering Laboratory
University of Delaware
Newark, Delaware 19716

ACKNOWLEDGMENTS

TABLE OF CONTENTS

Appendix

LIST OF FIGURES

LIST OF TABLES

ABSTRACT

In the world of civil and geotechnical engineering, remote sensing has the potential to replace in situ measurements of soils and sediments that are often unfeasible or lacking in spatial and temporal resolution. While visible band is, perhaps the most common form, it lacks the inherent properties of the thermal band which has proven itself in attaining material properties.

Ground based applications have increased in popularity due to their relatively low price and ease of setup. However, these applications are performed at a relatively low elevation and objects of interest may be a large distance away. Therefore, the images are obtained at oblique incident angles. The oblique incident angles have an effect on the emissivity and through it the observed temperature.

This project, unlike previous experiments, observed the effect of polar observation angle on emissivity, and through it the observed radiant temperatures, for both water and sand surfaces within a thermally controlled laboratory environment. The observations performed using a broadband (7.5-13μm) imager. The methodology was inverted and used to transform angular imagery to temperatures associated with observations normal to the material surface.

This project was extended further with a field application. On a bank of the Wolf River in Mississippi, thermal imagery was captured. Thermal diffusivities were calculated for various regions of interest from the thermal imagery. The remotely determined thermal diffusivities were validated by values obtained from methods that exclusively used in situ temperature measurements.

In summary, this project outlines the methods for using oblique, time-sequenced, remotely-sensed thermal imagery to obtain the thermal diffusivity of the observed material surface.

Chapter 1

INTRODUCTION

Modeling physical processes in the intertidal environment requires an understanding of the spatio-temporal distribution of sediments within the environment and their physical properties. In situ measurements are often difficult to collect and lacking in spatial and temporal resolution so efforts have turned to remote sensing as an alternative for obtaining this information.

Remote sensing has been successful in the investigation of the properties and behavior of water in the intertidal environment using visible band (RGB) imagery, 0.4-0.7μm. However, sediment often does not exhibit the same type of intensity variations as seen in the RGB imagery of water. Another option is time-sequenced thermal-infrared (TIR) imagery, 7.5-14μm, which may allow us to infer information regarding important land environment variables such as sediment lithology [Ninomiya et al., 2005], moisture content [Minacapilli et al., 2009; Mira et al., 2007] and potentially porosity.

Some aerial and satellite remote sensing applications lack the appropriate temporal or spatial resolution for tide dominated environments, due to the limited dwell time or observed area of the aircraft or probe. Other applications are complicated by variable geometric correction, due to the jitter of the aircraft, or unfeasible due to cost. Recently more emphasis has been placed on ground-based remote sensing (GBRS). GBRS applications are promising, but they are performed at a relatively low elevation and objects of interest may be a large distance away from

1

the imager resulting in highly oblique incident angles. The oblique incident angles have created additional difficulties because of the effect on emissivity.

There are a number of parameters that impact quantitative interpretation of TIR images, such as incidence angle, that need to be understood better before wide-scale application in the field environment. To address this issue, laboratory experiments have been conducted that simulate angular variations in sediment emissivity on the temperatures in TIR images [Cuenca & Sobrino, 2004; Kirbus et al., 2003; McAtee et al., 2003; Lagouarde et al., 1995; Labed and Stoll, 1991]. General trends have been consistent; however these studies did not investigate highly oblique incident angles and failed to account for some systematic measurement errors, such as reflections. In this work we systematically examine effect of highly oblique polar angles of observation on thermal imagery while isolating the effect by minimizing all possible thermal noise. Data are then used to validate a model that predicts the angular effect.

1.1 Thermal Imaging

Thermal imaging is passive and works by capturing the TIR radiation observed within the imager field of view. TIR is special because electromagnetic (EM) radiation in this band is emitted by a surface on an atomic scale. Imagers using other bands such as mid-infrared, near-infrared, and visible band capture the radiation that is reflected off of the surface. The exact internal mechanics of TIR imagers depends on manufacturer and model.

On a TIR imager, the lens focuses the electromagnetic radiation and is generally made of germanium that is transparent to TIR. Inside the imager EM radiation interacts with a phased array of infrared-detector elements. The elements

2

may be on one of three types of detectors. They may be composed of a photovoltaic material that is excited by photons and ejects electrons. From these electrons a voltage is determined. Another option is a photoconductive material that becomes more electrically conductive when it interacts with photons. From this conductivity a voltage drop is measured. These first two material types have strict cooling requirements to detect the photons and thus are not traditionally used for hand held TIR imagers. The third detector is called a microbolometer and does not require cooling. Microbolometers change their electrical resistance when they absorb thermal energy, which is then used to measure a voltage drop.

Voltages are converted to radiances [$Wm^{-2}sr^{-1}$] using a manufacturers calibration curve and user defined parameters (emissivity, distance to target, atmospheric temperature, relative humidity, and reflected temperature) to calculate object temperatures within the imager's firmware. Combining each detecting element results in a detailed pattern called a thermogram that is displayed. Radiance values are internally converted to temperature values using Planck's equation. Examples of these images are seen in Figure 1.1 and Figure 1.2.
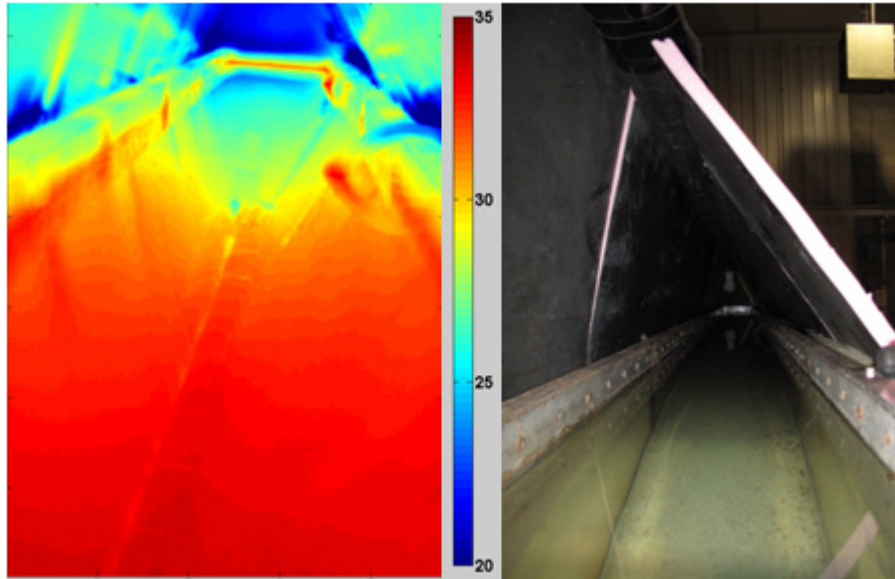
Figure 1.1: Example TIR Imagery (left, [°C]) for the Water Experiment with corresponding RGB Imagery (right) at ~80° from Nadir
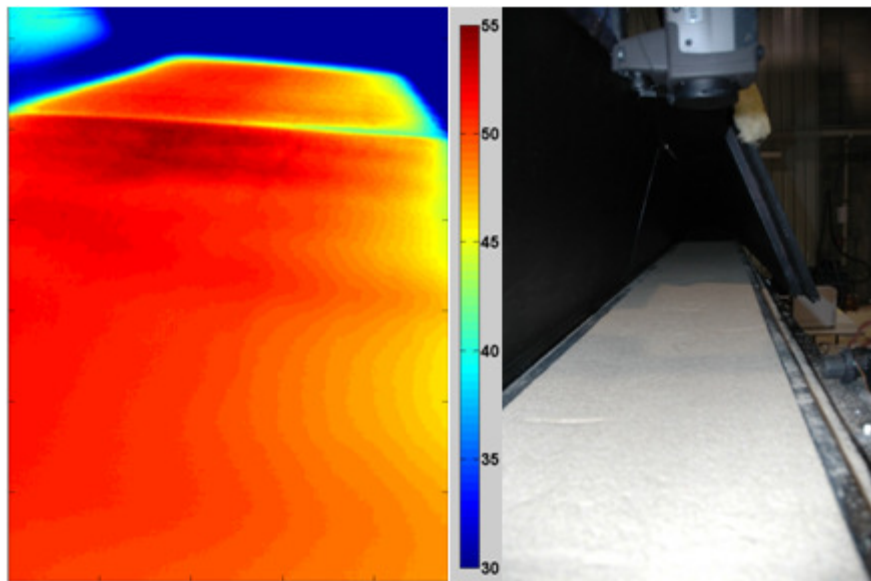
Figure 1.2: Example TIR Imagery (left, [°C]) for the Sand Experiment with corresponding RGB Imagery (right) at ~80° from Nadir

1.2   Emissivity and the Angular Effect

The radiant temperature of a pure, perfectly smooth material that is thick enough to be opaque is a non-linear function of its emissivity. Emissivity is the relative ability of a material's surface to emit radiation compared to a black body, a perfect absorber, at the same temperature and wavelength. Emissivity (ε) is a fundamental material property defined by the following equations [Modest, 2003; Kruse et al., 1962].

$$\varepsilon_{eff}(T) \equiv \frac{M_E(T)}{M_{E,bb}(T)} \quad , \text{Effective Hemispherical Emissivity (1.1)}$$

$$\varepsilon_{\lambda hem}(T) \equiv \frac{M_{E,\lambda}(T)}{M_{E,bb,\lambda}(T)} \quad , \text{Spectral Hemispherical Emissivity (1.2)}$$

$$\varepsilon_{\omega\lambda}(T,\hat{S}) \equiv \frac{M_{E,\omega,\lambda}(T)\cos(\theta)d\Omega}{M_{E,bb,\omega,\lambda}(T)\cos(\theta)d\Omega} = \frac{M_{E,\omega,\lambda}(T)}{M_{E,bb,\omega,\lambda}(T)} \quad , \text{Spectral Directional Emissivity (1.3)}$$

Here, effective hemispherical emissivity is the ratio of total emitted radiance into a hemisphere from a surface to the total emitted radiance into a hemisphere by a black body at the same temperature. The spectral hemispherical emissivity is similar to the effective hemispherical emissivity but for only the emitted radiance into the hemisphere between spectral interval λ to $\lambda+d\lambda$. Spectral directional emissivity is the ratio of the emitted radiance by a surface between spectral interval λ and $\lambda+d\lambda$ into the solid angle between ω and $\omega+d\omega$ for a specified direction vector $\hat{S}$ to the emitted radiance within the same spectral interval into the same solid angle and in the same direction by a black body at the same temperature. Emissivity and radiance are functions of temperature (T). All emissivities are always less than unity, except for the case of a black body which has an emissivity of unity. $\hat{S}$ is composed of a polar angle (θ) and an azimuth angle (ϕ), Figure 1.3. The work presented in this paper

considers the effect of polar angle on emissivity only. For optically smooth materials, azimuth angle should have no effect. However for real-world materials, especially under anisotropic loading, this may not be the case [Oren & Nayar, 1995].
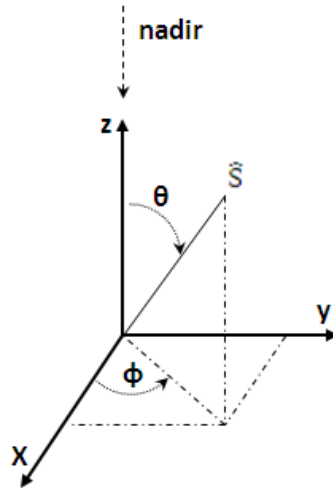
Figure 1.3:   Direction Vector and Coordinate System

One complication is that emissivity may be defined in terms of "power emitted" with units of Watts rather than emitted radiance. This distinction is significant when performing calculations. One can convert between radiance and power emitted if the surface area of the emitting surface and the solid angle being emitted into are known. For the calculations in this work only emitted radiance values are used.

Emissivity can also be understood in terms of Kirchoff's Law:

$$\varepsilon = \alpha \qquad\qquad (1.4)$$

This law is best understood with the situation of a small object within the walls of an evacuated cavity. Here there are two surfaces, that of the small object and that of the cavity. In this situation the net flow of radiation will move towards the cooler of the two. Once at thermal equilibrium the power radiated by the small object is the same power that is absorbed by it. This means that the absorptivity is equal to the emissivity of the object's surface and this holds true in all cases. If the object is a black body then both absorptivity and emissivity are unity. This is also true for every spectral component [Modest, 2003], and direction for most materials [Snyder et. al, 1998]:

$$\varepsilon_{\omega\lambda}(T, \hat{S}) = \alpha_{\omega\lambda}(T, \hat{S}), \tag{1.5}$$

where $\alpha_{\omega\lambda}(T, \hat{S})$ is the spectral directional absorptivity. Equation 1.5 can be used with the statement of conservation of energy:

$$\alpha_\lambda + p_\lambda + \tau_\lambda = 1, \tag{1.6}$$

where p_λ is spectral reflectivity and τ_λ is spectral transmissivity. Equation 1.6 indicates that the total amount of energy incident upon a material surface is eitherabsorbed, reflected, or transmitted through it. In this work, only thermally opaque materials are considered (τ_λ=0). Simplifying and applying Kirchoff's Law we obtain [Modest, 2003; Snyder et. al, 1998]:

$$\varepsilon_{\omega\lambda}(T, \hat{S}) = 1 - p_{\omega\lambda}^{\cap}(T, \hat{S}), \tag{1.7}$$

where $p_{\omega\lambda}^{\cap}(T, \hat{S})$ represents the spectral directional-hemispherical reflectivity.

It is also important to note that the ending "-ivity" is recommended for describing the radiative properties of pure, perfectly smooth materials and "-ance" for describing the radiative properties of rough and contaminated surfaces. Modest [2003] stated that this type of nomenclature is recommended by the National Institute of Standards and Technology. Often in the literature the "-ivity" terms (i.e. emissivity, reflectivity, absortivity, transmissivity) are used interchangeably and incorrectly with the "-ance" terms (i.e. emissance, emittance, reflectance, absorptance, transmittance). For example, when observing a perfectly flat surface of pure quartz the correct term would be emissivity. However, when observing a nearly flat surface of sand that has voids and impurities, the correct term would be emittance or emissance. The reason behind this terminological dichotomy is that for flat, pure materials the theory holds true while for real materials it is an estimate. In this work, we used "-ivity" terms throughout for discussing real materials. This was done for consistency and to make it easier on those unfamiliar with the nuances of electromagnetic theory.

Emitted radiance from a surface is a partition of the total radiance that is observed by an imager within the real world. This partitioning can best be described by Equation 1.8:

$$M_{tot} = M_E + M_P - M_{TR}, \tag{1.8}$$

where M_{tot} is the total radiance observed by the imager, M_E is the radiance emitted by the material surface, M_P is the radiance reflected off the surface, and M_{TR} is the radiance lost in the transmitting material, commonly air, and the emission from the

atmosphere into the imaging path. All variables have the units of radiance $[Wm^{-2}sr^{-1}]$. In the real world, the terms can vary with material, spectrum, angle, material temperature, ambient temperature, humidity, and time. When performing GBRS it is desirable to minimize and account for M_{TR} and M_P. Our approach to this minimization is explained in the following chapters.

It is clear from the above definitions that the orientation of the imager with respect to the surface normal (a.k.a. observation geometry) will affect emissivity, due to the observation angle, and in turn the temperature that is observed. In application it is desirable to remove this angular effect on the apparent temperature seen in the image. In removing the angular effect it may be possible to determine material boundaries and possibly material properties.

1.3   Previous Work

The inherent optical properties , in the thermal band, of few materials have been as extensively researched as the water surface [Hall, 1964; Querry et al., 1977; Takashimi & Takayama, 1981; Sidran, 1981; Masuda et al., 1988; Rees & James, 1992; Bertie & Lan, 1996; Watts et al., 1996; Wu & Smith, 1997; Niclos et al., 2005]. This has primarily been driven by a need to accurately capture the sea surface temperature for climate research.

There remains a pressing need to quantify optical properties and directional viewing effects in land surface temperature (LST) measurements. The angular effect has been documented for water and ice surfaces [Rees & James,1992], snow [Dozier & Warren, 1982], opaque materials [Vitkovskii et al., 2009], forest vegetation [Kimes et al., 1981; Balick & Hutchinson, 1986] and sediments [Labed & Stoll, 1991; Lagouarde et al., 1995; Snyder et al., 1997; McAtee et al., 2003; Cuenca

& Sobrino, 2004; Cuenca et al., 2005]. For sediments, the observations have consistently shown a general trend that emissivity decreases as observation angle becomes more oblique, especially at angles greater than 45° from nadir. This angle may be related to the material's Brewster's angle [Hall, 1964], which deals with the polarization of the reflected radiation. Unfortunately, there are few observations for very oblique angles (>70° from nadir). Typical GBRS applications use hand held or tower mounted imagers and require observation angles that may approach 90° from nadir. Therefore it is important that these highly oblique angles be thoroughly examined to quantify the effect on emissivity variation.

One model has been developed to describe the directional thermal emission from a snow surface [Wiscombe and Warren, 1980; Dozier and Warren, 1982]. The model stems from δ-Eddington approximation [Joeseph et al., 1976] for multiple scattering and from Mie theory for single scattering. Although this model was developed for snow, it was pointed out that Mie theory is suitable for particles composed of diameters within $10^{-2} - 10^2$ μm, which is applicable to soil particles [Richter, 1962]. So, the model was implemented for sediments [Ishida et al., 1991; Li et al., 1999; and McAtee et al., 2003]. This model did capture the general trend that emissivity decreases with increasing polar angle, however a simpler methodology was chosen for this study. Furthermore, the model was inaccurate when the sun was present [McAtee et al., 2003] because the model did not account for anisotropy of the downwelling radiation that was observed. In other words, the change in land surface brightness temperature with polar angle that was seen during the day was not solely dependent on the optical properties of the soil but also on the heterogeneity of solar input.

10

It is plausible that the reason a robust model for capturing the angular effect on emissivity in sediments does not currently exist in the literature is because of systematic errors in the measurements. For example, past experimental setups showed no attempt to insulate the apparatus [Sobrino & Cuenca, 1999; Cuenca & Sobrino, 2004; Cuenca et al., 2005]. Therefore, the apparatus undoubtedly caused unquantifiable reflections that would have been seen as noise in the measurements. Furthermore, the sky was assumed to be diffuse. This assumption ignored the well-known directional variation of the downwelling radiation, thus the substitutions in the derivation of their first equation [Sobrino & Cuneca, 1999] were invalid [Kirbus et al., 2003]. Rees and James [1992] attempted to measure actual background radiation corresponding to specular reflections into the angle of observation. However, measurements were only for some angles and for most of the angular range extrapolation was used [Kirbus et al., 2003].

A number of other complications may introduce noise into the measurements. One issue for small-scale experiments is narcissus, which is the reflection of the IR detector on itself when readings are taken normal to a surface. There is also the issue of an optically rough surface, caused by grain size and porosity. Heterogeneity can lead to analytical errors if the different sediments, each with different emissivity, are not analyzed separately. Outdoors the sun can cause different results for each solar angle. Lastly, shadows and reflections can create noise in measurements and create temporal variability.

Chapter 2

RADIATIVE MECHANICS

Through use of the theory presented in this chapter, it is possible to predict a TIR image observation for any observation geometry. Given that the surface being observed is flat and dielectric. In the following chapters these calculations were validated by comparison to laboratory data for both water and sand surfaces. Afterwards the process was inverted to convert the temperatures observed with oblique observation geometry to the temperatures associated with nadir observation geometry.

2.1 Predicting Emissivity

The emissivity of a flat and dielectric surface may be predicted by referring to Equation 1.7. For this chapter we will simplify the notation and begin with a reconstruction of Equation 1.7.

$$\varepsilon_\theta = 1 - p_\theta \tag{2.1}$$

Here ε_θ refers to the angular emissivity and p_θ refers to the angular reflectivity. These are material properties that are specific to the wavelength of the EM spectrum (λ), the direction vector ($\hat{S}$), and the material temperature (T). The emissivity of the water surface is commonly given as 0.98, which means that the reflectivity is small. However, this value is specifically for a nadir measurement. As the polar angle (θ) moves away from nadir the emissivity decreases and the reflectivity increases. Additionally, broad band sensors may be imaging across a band that contains

significant emissivity variability for a particular material. Averaging is then performed to obtain an effective emissivity.

Most sensors, including the one we used in this study, are unpolarized (having no preference to either polarization). So, the total reflectivity can be defined as [Modest, 2003]

$$p = \frac{|p_{\parallel}|^2 + |p_{\perp}|^2}{2} \tag{2.2}$$

If the surface is characterized as a dielectric, the light reflecting from the surface has a polarization of both parallel ($\parallel$) and perpendicular ($\perp$). These reflectivities can be predicted by the Fresnel Relationships [Takashimi & Takayama, 1981; Masuda et al., 1988; Wu & Smith, 1997; Modest, 2003].

$$p_{\parallel} = \left(\frac{\cos\theta_2 - n*\cos\theta_1}{\cos\theta_2 + n*\cos\theta_1}\right)^2 \tag{2.3}$$

$$p_{\perp} = \left(\frac{\cos\theta_1 - n*\cos\theta_2}{\cos\theta_1 + n*\cos\theta_2}\right)^2 \tag{2.4}$$

Here n is a complex index of refraction of the material, defined as

$$n = \eta - iq \tag{2.5}$$

θ_1 is the incident angle and θ_2 is the angle of transmission. These angles are displayed in Figure 2.1. They are related according to Snell's law of refraction.

$$\sin\theta_1 = \eta * \sin\theta_2 \tag{2.6}$$
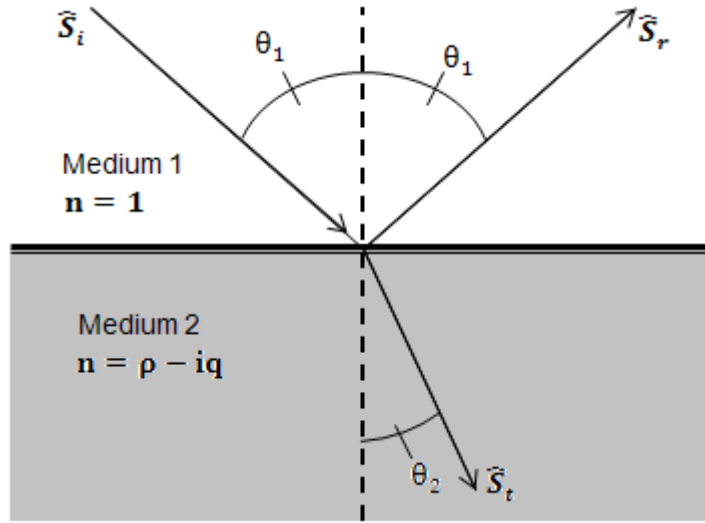
Figure 2.1:   Geometry of Reflection. $\hat{S}_i$ is the incident light radiation. $\hat{S}_r$ is the reflected radiation. $\hat{S}_t$ is the transmitted (refracted) radiation.

The index of refraction, in the thermal band, for water and sand can be determined from the literature. The incident angle (θ) can be determined from the observation geometry of the imager during an experiment. θ is used for θ_1 within the calculations. Knowing these values it is possible to predict the directional emissivity based on the above equations.

2.2   Attaining Radiant Temperature from Emissivity

The predicted radiant temperature seen by the imager at polar angle θ (T_θ) can be obtained from predicted emissivity (ε_θ) through the use of the Stefan-Boltzmann law. The equations are as follows:

$$T_\theta = \left(\frac{M_{IM,\theta}}{\varepsilon_N * \sigma}\right)^{\frac{1}{4}} \tag{2.7}$$

$$M_{IM,\theta} = M_{tot,\theta} - M_{P,N} \tag{2.8}$$

$$M_{tot,\theta} = M_{E,\theta} + M_{P,\theta} \tag{2.9}$$

$$M_{E,\theta} = \varepsilon_\theta * \sigma * T_o{}^4 \tag{2.10}$$

$$M_{P,\theta} = (1 - \varepsilon_\theta) * \sigma * T_P{}^4 \tag{2.11}$$

$$M_{P,N} = (1 - \varepsilon_N) * \sigma * T_P{}^4 \tag{2.12}$$

In this set of equations σ is the Stefan-Boltzmann constant 5.67e-8 $Js^{-1}m^{-2}K^{-4}$. ε_N is the predicted emissivity at nadir. $M_{IM,\theta}$ is the radiance used by the imager to determine T_θ. $M_{tot,\theta}$ is the total radiance captured by the imager at θ. $M_{E,\theta}$ is the radiance emitted by the surface at θ. $M_{P,\theta}$ is the radiance reflected off the surface at θ. $M_{P,N}$ is the radiance reflected off the surface at nadir. All radiance values have units of $Wm^{-2}sr^{-1}$. T_P is the reflected temperature and T_o is the object temperature. All temperatures have units of K.

Reflected temperature and object temperature are measured values. Typically reflected temperature is taken as the ambient air temperature. The object temperature can be given by the imager at nadir or kinetic temperature. The imager used in this study internally removes the radiance associated with the reflections at nadir. This is why $M_{P,N}$ is subtracted in equation 2.8 to properly predict the temperature that the imager would display at θ.

Using the above equations it is possible to predict the temperature that the imager will display at some angle θ for a given surface. The process can be reversed, using the angular imager measurements to predict the surface radiant temperature at nadir, something that is desirable for highly oblique experimental imagery.

Chapter 3

EXPERIMENTAL SETUP AND PROCEDURE

Traditionally the approach to gathering angular GBRS data is through one of three methods. The target can be placed in an enclosure and rotated with respect to the imager [Vitkovskii et al., 2009]. However this would require a small target and would not work in the field environment. The imager can be placed on a mount that tilts [Balick & Hutchinson, 1986; Rees & James, 1992; McAtee et al., 2003]. However this means that the distance to the target is changing and that the material within the imager's field of view (FOV) may be changing. The third option is to use a goniometer [Labed & Stoll, 1991; Lagouarde et al.,1995; Cuenca et al., 2005]. A goniometer, as seen in Figure 3.1, maintains a constant distance between the imager and the target, it can be setup in the field environment, and most of the material seen at nadir will remain in the FOV for all θ.
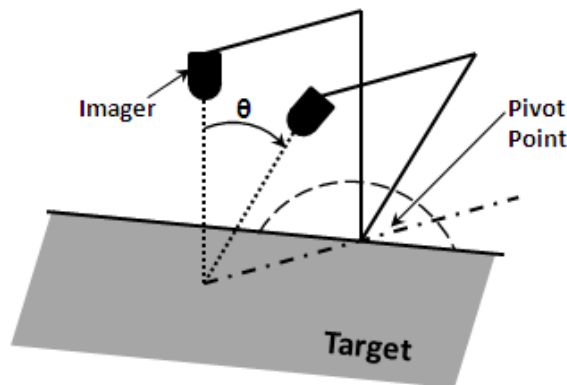
Figure 3.1: General Goniometer Diagram.

This chapter details the methodology used for collecting measurements for both water and sand surfaces as well as the geometry used for analyzing the data by pixel. The raw data obtained for both experiments is available in appendix III.

3.1   Experimental Setup

The FLIR was attached to a custom designed apparatus that can best be described as a quasi-goniometer, shown in Figure 3.2. It is not a true goniometer because the pivot point is above the target surface, which means the distance from the imager to the target changes with θ. However, the true distance was determined based on the geometry of the setup. Furthermore, the intersection angle between the ray projected from the center of each pixel and the target surface was calculated by knowing the FOV of the FLIR, the focal distance of the FLIR, and the number of pixels in the FLIR. This is clarified by figures later in this chapter. The goniometer was attached to a laboratory water flume so a long surface could be imaged. This plays an important role at oblique angles as more of the surface is viewed.

The initial experimental setup was used for the examination of a flat water surface, described in section 3.1.1. The setup was later improved and used for the examination of a flat sand surface, described in section 3.1.2.

3.1.1   Setup for the Water Experiment

The goniometer, Figure 3.2, was attached to the flume, Figure 3.3, such that as it was rotated about the pivot point more flume was viewed. The FLIR was oriented such that it recorded imagery at 240 pixels across the width of the flume by 320 pixels along the length of the flume. The flume had inside dimensions of 5.49m long by 0.30m wide by 0.55m high. Two other significant dimensions are called out

17

in Figure 3.3 and are later used in the calculations. Those other dimensions are the height from the water surface to the pivot point (H_P=108mm to 120.6mm; variation is due to leaks in the flume) and the length of the goniometer arm from the pivot point to the FLIR lens (L_G=260.35mm). Both figures label the insulation that was implemented. Above the flume 8'x4' sheets of 1" thick rigid, cellular polystyrene thermal insulation were coated with Rust-Oleum K7776 flat black protective enamel paint and suspended from a metal bar that ran the length of the flume. The painted insulation created a more thermally homogenous environment. The bar running the length of the flume was covered with black foam pipe insulation. The sides of the flume were covered with fiberglass insulation, Figure 3.3, to minimize cooling of the water.

A number of measurement devices were used beyond the FLIR itself. 16 kinetic temperature sensors, arranged in two arrays of 8, were submerged at roughly one third and two thirds the length of the flume. These temperature sensor arrays gave insight into the actual water surface temperature. A relative humidity (RH) probe was suspended from the top bar at the back of the flume. This probe captured the RH and air temperature within the insulated environment. 6 additional kinetic temperature sensors were left out in the lab itself to understand the surrounding air temperature. Also, the IR thermometer was used to capture near nadir radiant temperatures of the water surface.
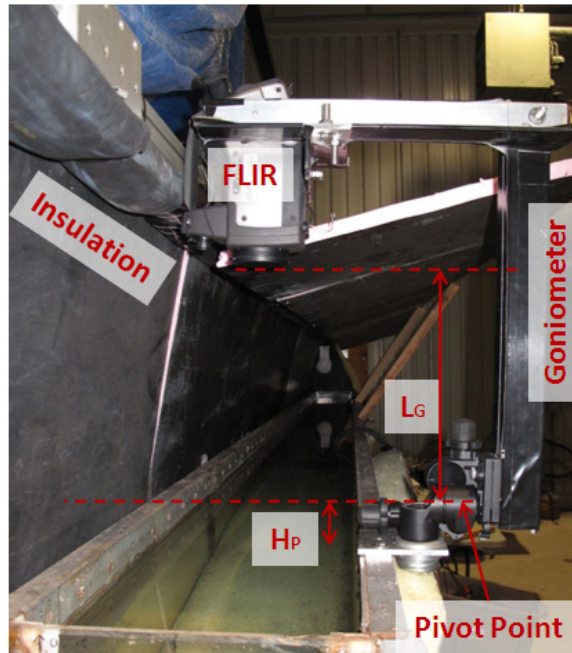
Figure 3.2: **Goniometer for Water Experiment**
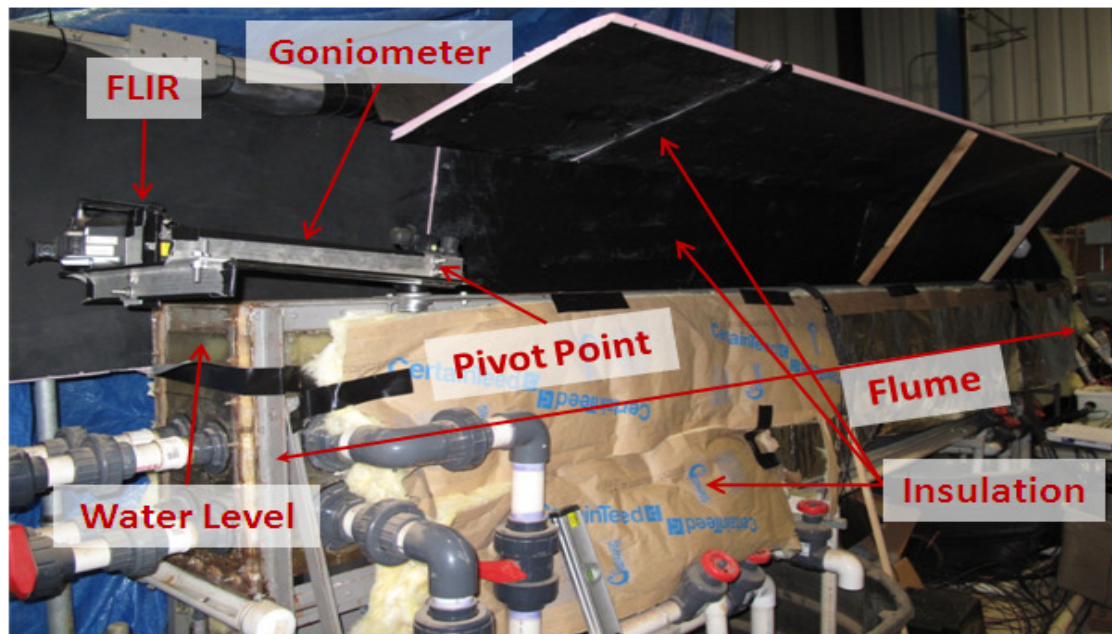
Figure 3.3: **Apparatus for the Water Experiment**

3.1.2   Setup for the Sand Experiment

The goniometer, Figure 3.2, was attached to the flume, Figure 3.3, such that as it was rotated about the pivot point more flume was viewed. The FLIR was oriented such that it recorded imagery at 240 pixels across the width of the flume by 320 pixels along the length of the flume. In Figure 3.4 the height from the sand surface to the pivot point (H_P) is 28.58mm, while L_G remains the same as the water experiment. Both figures label the insulation that was implemented. Strips of the rigid insulation were coated in the same flat black protective enamel paint and suspended beneath the metal bar, seen in Figure 3.5. These strips insulated the bar and had an identical emissivity to the suspended side panels thus creating a more thermally homogeneous environment than the water experiment.

In this experiment, dry sand was heated from below by Omega Engineering SRMU021248 heating blankets. The sand had a porosity (ζ) of 36% with ~1% uncertainty; additionally a sieve analysis of the sand can be seen in Figure 3.6. The blankets and sand were placed within a wooden container, or "sled," that could be moved down the length of the flume. The raised edges of the sled allowed for the creation of a flat surface. The top of the flume itself was covered with sheets of ½" plywood that were coated with the same flat black protective enamel that coated the insulation.

Similar to the water experiment, a number of other measurement devices were used. Kinetic sensors were placed at four locations above the top strips of insulation at various intervals along the length of the flume, the location nearest to the imager also held the RH probe. Kinetic temperature sensors were also mounted at four locations below the top edge of the flume where it met the suspended side panels; they were placed at intervals corresponding to the top sensors. Eight other kinetic

temperature sensors were left out in the lab to collect the surrounding air temperature. Temperature data were collected for the Omega thermocouples used by the Omega temperature controller for the heating blankets. Also, the IR thermometer was used to capture near nadir radiant temperatures of the sand surface.
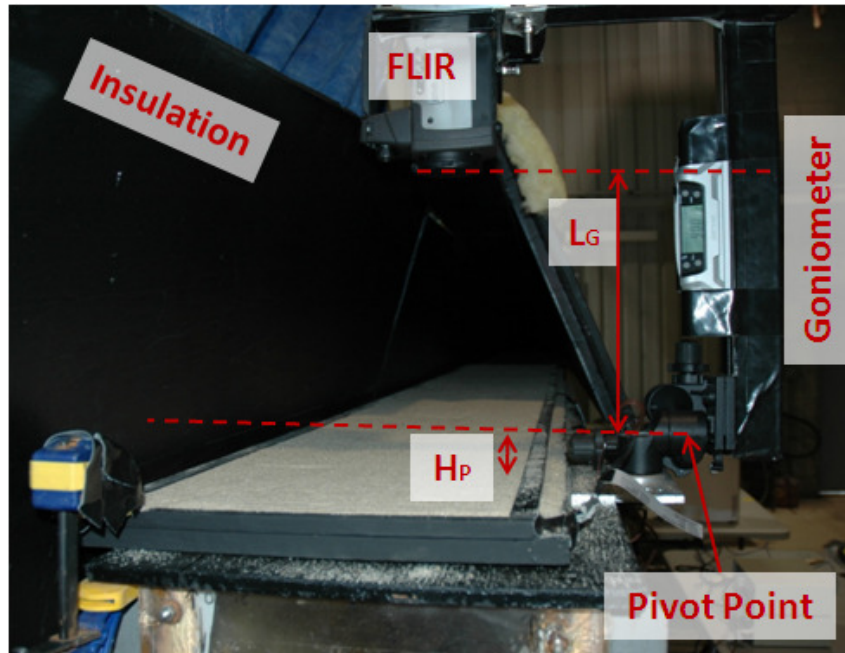
Figure 3.4:   Goniometer for Sand Experiment
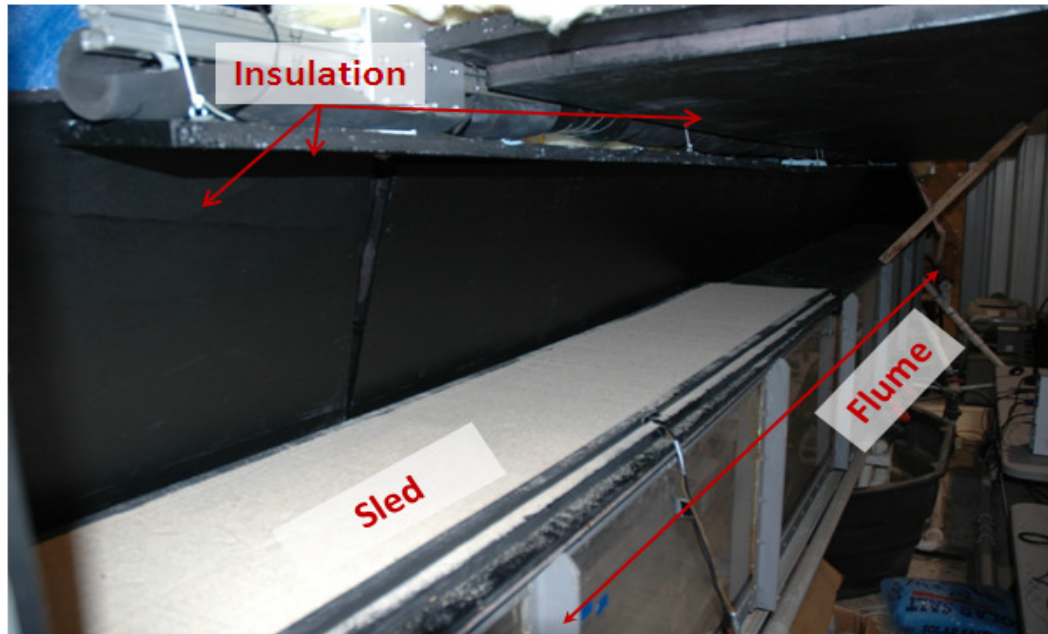
Figure 3.5:   Apparatus for the Sand Experiment
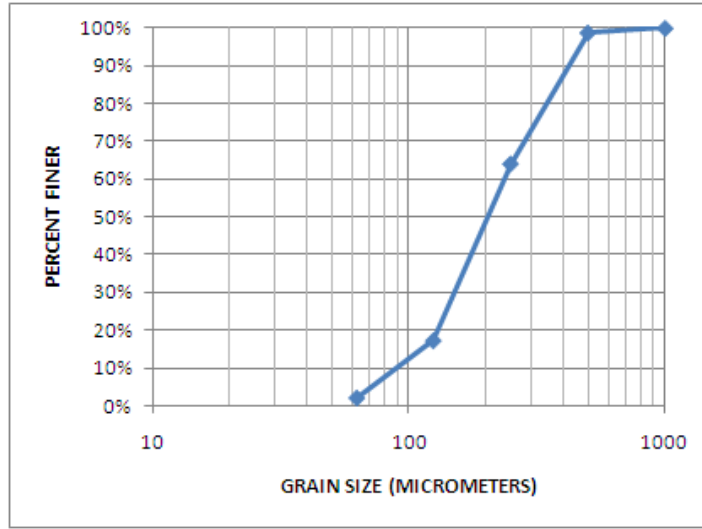
Figure 3.6:   Sand Sieve Analysis

It is important to note that the sand appeared as a rough surface in the imagery because of the wavelengths captured by the FLIR (7.5-13μm) and the grain size of the sand (Figure 3.6).

3.2   Measurement Device Descriptions

Multiple types of sensors were used to collect measurements during the experiment.

3.2.1   FLIR Imager

A FLIR Systems P45HSV thermal camera was used for the experiments. The specifications for this handheld forward looking infrared radiometer (FLIR) are in Table 3.1.

Table 3.1: FLIR Specifications

Manufacturer	FLIR Systems
Model	P45HSV
Spectrum	7.5-13μm
Detector Type	Focal plane array of uncooled microbolometers
Pixels	240 by 320
Instantaneous Field of View	1.1mrad
Field of View	14° (for 240) and 19° (for 320)
Temperature Range	-40°C to +500°C
Accuracy	±2°C or ±2%
Sensitivity	50mK at 30°C

The FLIR was set to an emissivity of unity throughout imagery collection during both experiments. This setting was chosen for experimental simplicity and was modified, along with other parameters, during the imagery post-processing.

3.2.2   Kinetic Sensors

Sensors ran off a Campbell Scientific CR1000 measurement and control system, using a Campbell Scientific AM16/32 relay multiplexor, a Campbell Scientific CFM100 compact flash module, and a Campbell Scientific SM4M/SM16M storage module. 24 Dynamax TM10 temperature probes, Figure 3.7, were employed along with a Campbell Scientific HMP50 temperature and relative humidity probe. The sensors collected readings every 5 seconds and recorded one minute averages of those readings.

Figure 3.7: **Campbell Scientific Datalogger (top) and Temperature Sensors (bottom)**

3.2.3 Omega Engineering Thermocouples

Two heat blankets were used in an effort to maintain a constant sediment temperature. The blankets were controlled using Omega Engineering CN7823 thermal controllers and Type K thermocouples, Figure 3.8. The sensors recorded measurements every 5 seconds and logged to a computer. Additionally, manual recordings of the temperature reading on the thermal controller display were recorded throughout the experiment, namely at the end of each image set.

Figure 3.8: Omega Temperature Controllers (top) and Thermocouple (bottom)

3.2.4 Fluke 561 IR Thermometer

Manual readings using an IR thermometer, Figure 3.9, were taken throughout the experiments. The IR thermometer works by focusing the infrared energy from a particular area, or spot size, onto a detector where it senses the energy. The spot size grows with distance. A distance of 300mm results in a spot diameter of 38mm while a distance of 900mm results in a spot size of 75mm. The specifications for this IR thermometer are in Table 3.2.

Table 3.2:   IR Thermometer Specifications

Manufacturer	Fluke Corporation
Model	561 IR Thermometer
Spectrum	8-14µm
Temperature Range	-40°C to +550°C
Accuracy	±1°C or ±1%
Response Time	500ms
Distance to Spot Size	12:1
Emissivity Settings	low(0.3), medium(0.7), high(0.95)

The IR thermometer was used along with a custom mount to provide more consistent

near nadir measurements. An observation angle of roughly 25° was used so that any

reflections from the measurer's hand were not within the spot size. The mount kept

the IR thermometer at a distance of roughly 350mm from the target surface.

Understanding the nadir or near nadir temperature plays a significant role in later

calculations where the surface temperature must be known.

Figure 3.9:   Fluke 561 IR Thermometer

3.3   Measurement Device Calibrations

When capturing multiple temperature measurements, determining the true temperatures is crucial and therefore device calibrations are significant. The following describes how the instruments were calibrated.

3.3.1   Kinetic Sensors

The Dynamax temperature sensors were placed in Fisher Scientific Model 90 water bath. The water bath, stable within 0.1°C, was set to a specific temperature. Once the temperature stabilized, readings were taken from the Campbell sensors as well as a manual thermometer. This was repeated for a number of temperatures ranging from 5°C to 50°C. Each sensor's data was plotted against the thermometer's. From this, a linear calibration was generated for each sensor. Every calibration had a coefficient of determination (R^2) that ranged from 0.9997 to 0.9999. For sensor specific values refer to Appendix II.

3.3.2   Omega Engineering Thermocouples

Thermocouples were used in the control of the thermal blankets for the sand experiment and were recorded throughout it. The same procedure followed for the kinetic temperature sensors was followed for the Omega thermocouples. This was done for temperatures from 4°C to 95°C. The R^2 for the linear calibrations were 0.99 for both sensors. The calibrations are located in Appendix II.

3.3.3   Fluke 561 IR Thermometer

Due to the high, near black body, emissivity of the water surface the calibration for the IR thermometer in the water experiment was determined using nadir measurements of the water surface from both the IR thermometer and the FLIR. The

IR thermometer had three emissivity settings; for this experiment it was set to high emissivity (equivalent to 0.95 as per manufacturer). FLIR images were taken at nadir using an emissivity of 0.98, a reflected temperature and atmospheric temperature equal to the environmental air temperature, RH was set to the environmental air temp, and a distance determined by the geometry. An average temperature was found for the nadir FLIR imagery and was considered the true surface temperature. An average temperature was also determined for the temperature range captured by the IR thermometer at nadir. Subtracting the average IR thermometer temperature from the true temperature, or average FLIR temperature, resulted in a correction of -1.5°C for the water experiment.

Again, finding the value for the sand experiment was more complex than the water experiment. Due to the lower emissivity of the sand surface, a temperature reference emitter (TRE) was custom-fabricated to replicate a black body surface, Figure 3.10. The emitter was made from solid copper with a milled internal channel. A constant temperature was maintained by a Fisher Scientific Model 90 water bath that circulated water through the channel. The surface was coated with Krylon flat black paint (ε=0.96). Insulation was utilized around the TRE to minimize thermal reflections. A Dynamax TM10 temperature probe was inserted into both the TRE and the water reservoir of the water bath and data were recorded on a data logger.
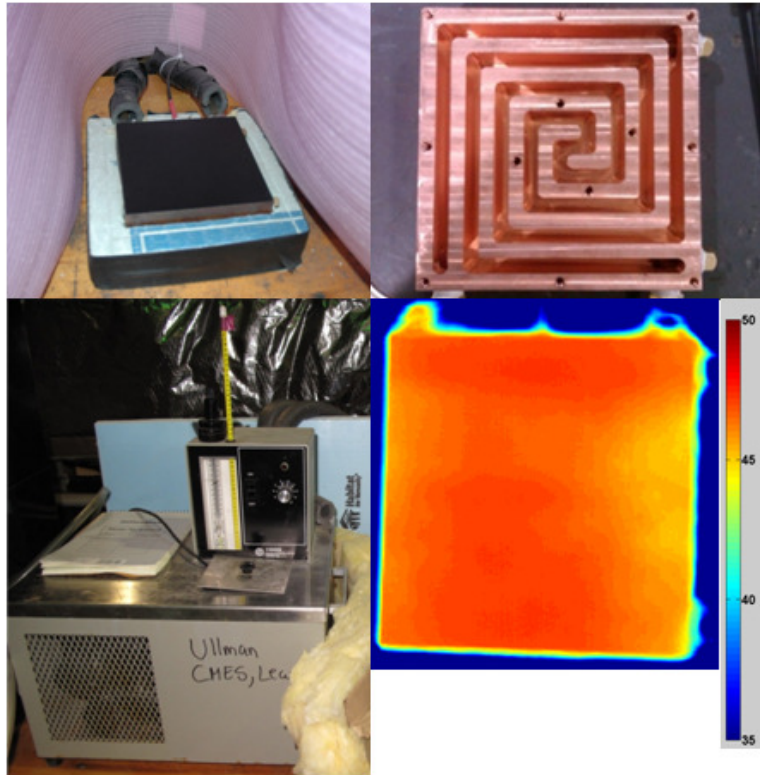
Figure 3.10: TRE Surface (top left), TRE Inside (top right), TIR Image of TRE (bottom right [°C]), and Water Bath (bottom left)

FLIR images of the TRE were taken at nadir using an emissivity of 0.96, reflected temperature and atmospheric temperature were set to the environmental air temperature, RH was set to the environmental RH, and a distance determined by the geometry. An average temperature of a region in the center of the TRE was found for the nadir FLIR imagery. The IR thermometer was again set to the high emissivity setting (ε=0.95) and an average temperature was determined for the temperature range captured by the IR thermometer at near nadir. The kinetic temperature probe inside the TRE was calibrated and considered the true surface temperature. Subtracting the FLIR average from the kinetic temperature resulted in a temporary FLIR calibration,

or "FLIRc." Similarly, subtracting the IR thermometer average from the kinetic temperature resulted in a temporary IR thermometer calibration, or "FLUKEc." Subtracting FLUKEc from FLIRc resulted in 0. So, for the sand experiment there was no calibration required for the IR thermometer. This was reinforced when we simply subtracted the IR thermometer average from the FLIR average and again received 0.

3.4 Experimental Procedure

The experiments were conducted at night in the Ocean Engineering Laboratory at the University of Delaware. Performing the experiments at night insured the walls and roof would be at a more stable and lower temperature. All the lights and heaters inside of the lab were turned off two or more hours before the experiments began.

Throughout this section the measured data are presented. Time series plots of the calibrated measured data for the two experiments can be found in Appendix III.

3.4.1 Water Experiment Procedure

For the water experiment, warm water (~36°C) filled the flume until it reached 108mm below the pivot. The water was mixed thoroughly before beginning the experiment to prevent any thermal gradients that may have existed along the length of the flume. The water was roughly 16°C warmer than the ambient air temperature. Note that for this experiment the water monotonically cooled to ~34°C, Figure III.1, the water level was lowering, and the ambient air was changing. However, all these changes were small, measured, and accounted for. Figure 3.11 displays the manual measurement procedure followed during the water experiment. The procedure began

at an observation angle of 85° from nadir and was repeated, in the following order, for 80°, 75°, 70°, 65°, 60°, 55°, 50°, 45°, 40°, 30°, 20°, 10°, and 0° from nadir. The kinetic sensors were auto-logging throughout the experiment.
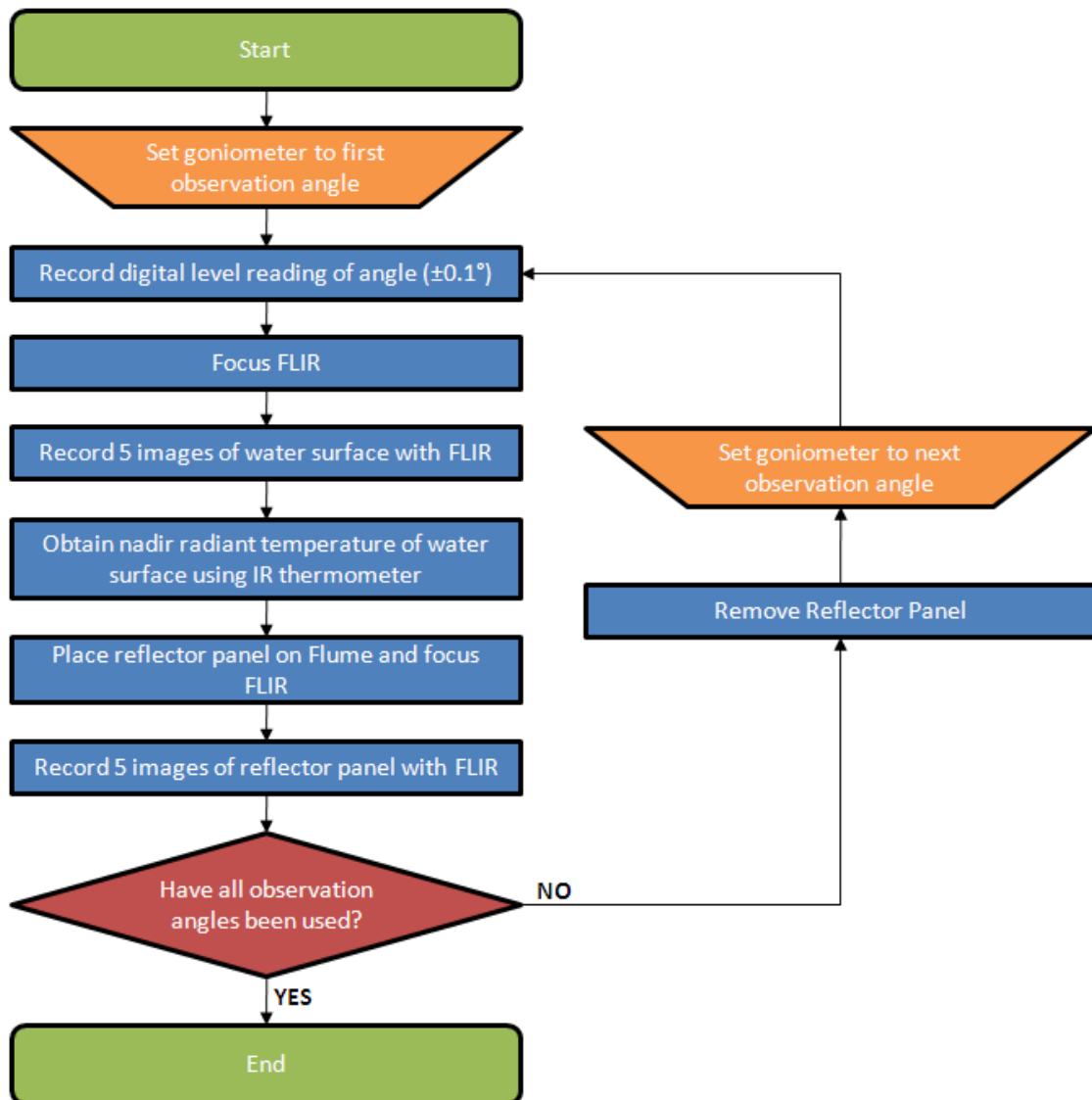
Figure 3.11: Water Experiment Manual Measurement Procedural Flow Chart

3.4.2 Sand Experiment Procedure

For the sand experiment the sand was dry and heated to maintain a stable surface temperature of 52°C and was 24°C warmer than the ambient air temperature. Figure 3.12 displays the manual measurement procedure followed during the sand experiment. The procedure began at an observation angle of 0° from nadir and was repeated, in the following order, for 20°, 30°, 40°, 50°, 60°, 65°, 70°, 75°, 80°, 85°, and 20° from nadir. The mounts described in Figure 3.12 kept the FLIR and Fluke at consistent angles of roughly 25° from nadir, where narcissus does not occur. It was also necessary to use multiple focuses at oblique observation angles to fully capture the observable surface in focus. The kinetic sensors were auto-logging throughout the experiment.
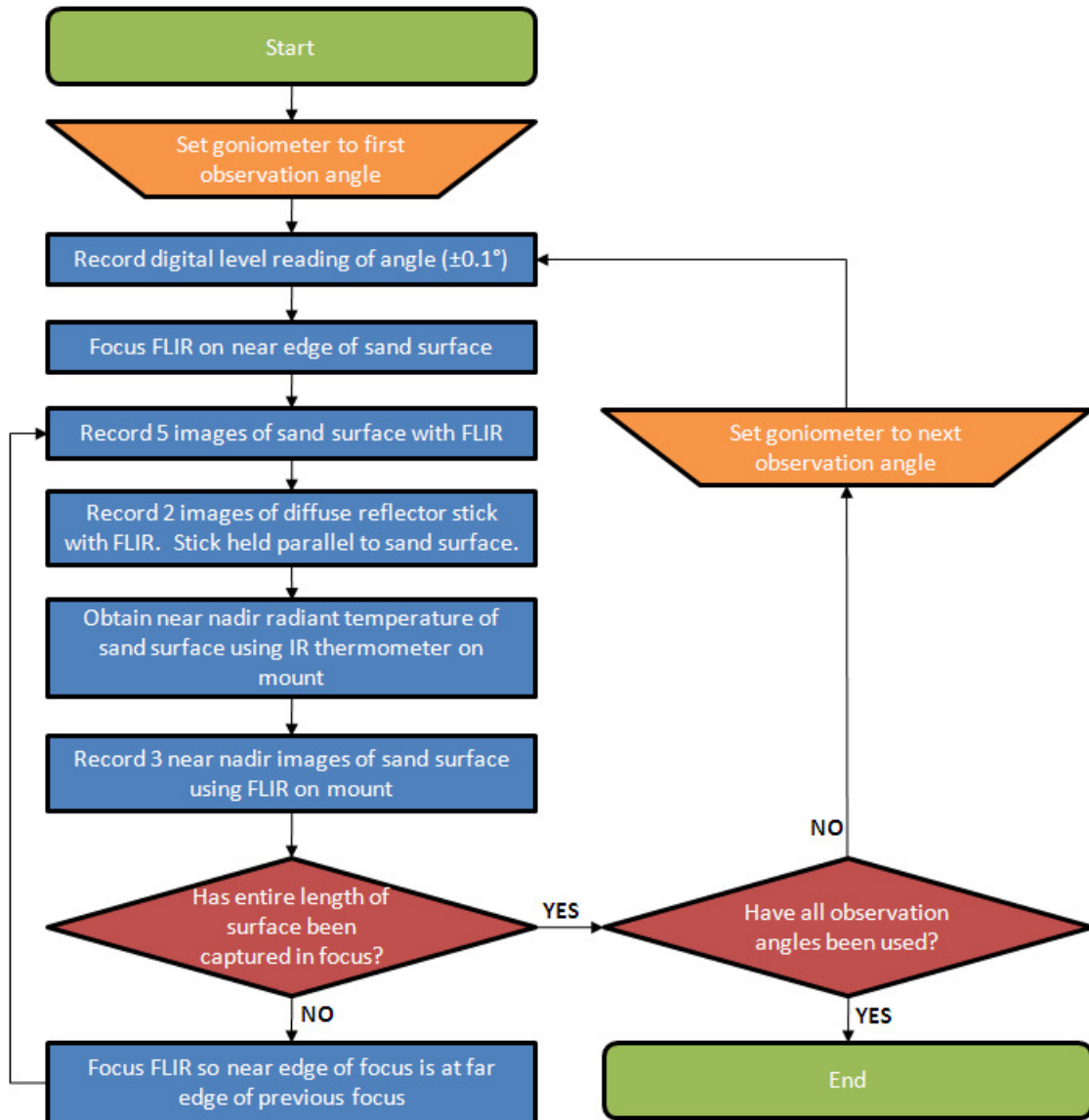
Figure 3.12: Sand Experiment Manual Measurement Procedural Flow Chart

3.5   FLIR Post-Processing

The FLIR imagery was originally recorded with an emissivity setting of unity for experimental simplicity. It was necessary to return to the images using FLIR Systems Researcher software and modify this value, as well as others that become

important when emissivity is no longer unity. By modifying these values the temperatures in the images were corrected.

Emissivity for the water experiment was chosen as 0.98. This value is well known for being the nadir emissivity of the water surface [Hall, 1964; Takashimi & Takayama, 1981; Sidran, 1981; Masuda et al., 1988; Rees & James, 1992; Watts et al., 1996; Wu & Smith, 1997; Niclos et al., 2005]. This value was also calculated as the average across the spectral range of the FLIR using data from NASA's Moderate Resolution Imaging Spectroradiometer (MODIS), Figure 3.13.
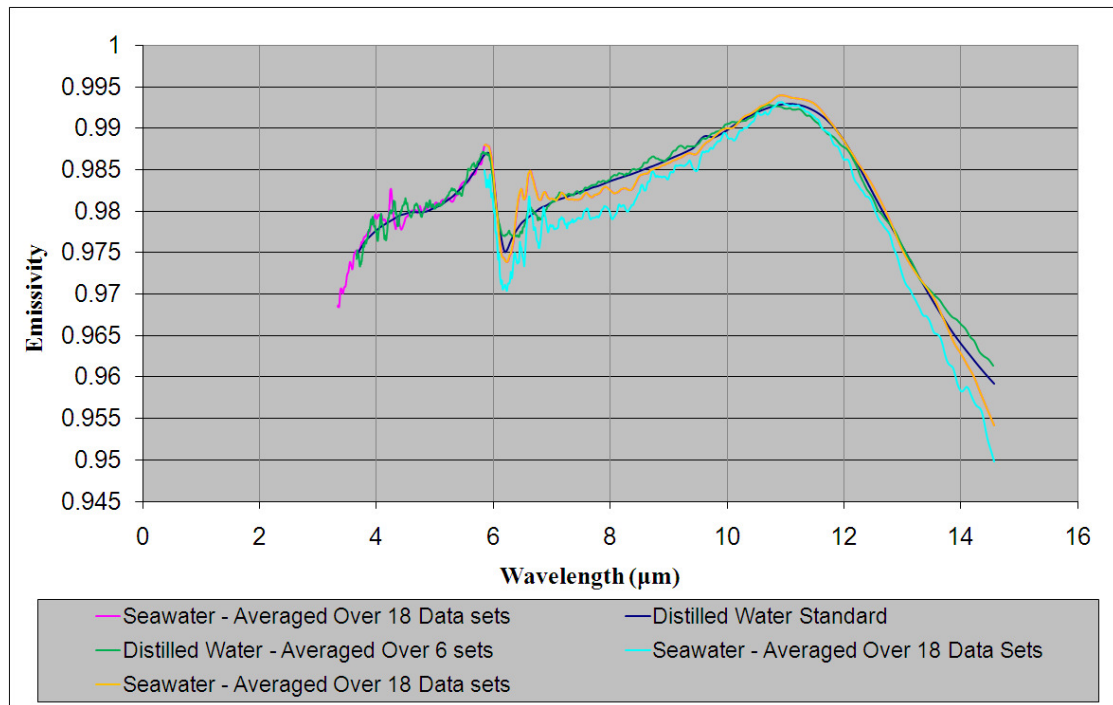
Figure 3.13: Spectral Emissivity of the Water Surface at Nadir

Choosing an emissivity for the sand experiment was more complex. We performed a test by having the FLIR at near nadir (~25°) looking down at the sand surface being heated. Omega sensor one was near the blanket and controlled the heating cycle. Omega sensor two was near the sand surface. The blanket was set to a specific temperature. Once the radiant temperatures stabilized, images from the FLIR and readings from the Omega sensors were recorded. Multiple stable temperatures were captured, spanning a range from 42°C to 95°C. The readings from the Omega sensor at the surface were calibrated and considered the true temperature of the sand surface. In the FLIR images, atmospheric temperature was set to the calibrated air temperature measured by the kinetic temperature sensors. The reflected temperature was set to the mean value obtained from a reflective surface in the images. Relative Humidity (RH) was set to the value obtained by the Campbell Scientific RH sensor. Lastly, distance was set for the length from the lens to the sand surface. In the FLIR software it is possible to highlight a Region of Interest (ROI) and calculate an emissivity by inputting the ROI's true temperature. This procedure was done for the sand surface using the calibrated Omega sensor data as the ROI's true temperature resulting in emissivity values for a range of temperatures, Figure 3.14.
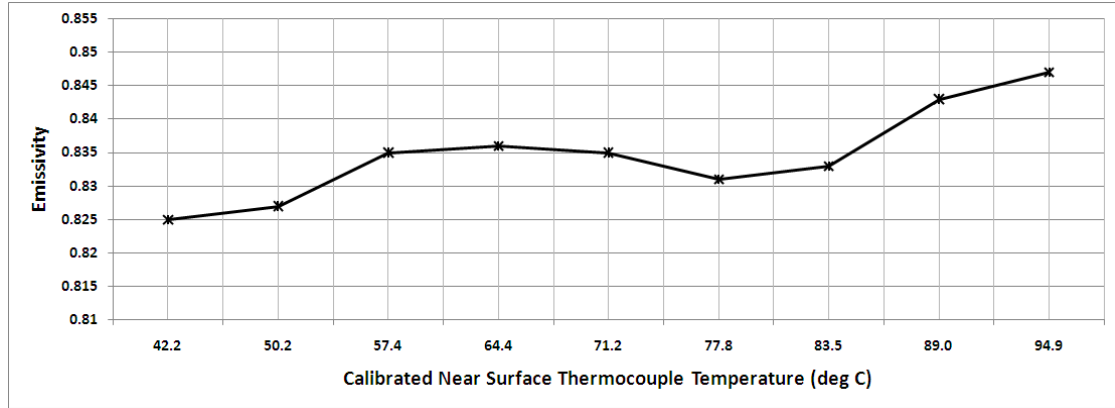
Figure 3.14: Nadir Emissivity of Sand Surface

Using these emissivity values, the nadir emissivity of the sand surface, for the temperature of the actual sand experiment (~52°C), was linearly interpolated. The value obtained for sand was 0.83. Fuchs and Tanner [1968] found an emissivity of 0.88 for course quartz sand with a volumetric water content of 0.7% in the 8-13μm wavelength. Hully et al. [2010] found an emissivity of 0.885 for dry sand in the 8.6μm wavelength and 0.953 for dry sand in the 11.3μm wavelength. Also, Qin and Karnieli [1999] found emissivities between 0.891 and 0.913 for natural sand surfaces in the 8-14μm wavelength. The literature values are slightly larger than the present values. It is noted, that past work did not provide detailed analyses of the sand samples and grain size distribution may have an effect.

In the imagery of the actual experiments the atmospheric temperature and the reflected temperature were chosen as the flume air temperature measured by the calibrated kinetic temperature sensors. The RH was set to the value obtained by the Campbell Scientific RH sensor. Also, distance was set as L_T, described later in section 3.5.

3.6   Geometry Calculations

3.6.1   Preparing the Imagery

Each observation angle and focus (in the case of the sand experiment) had a 5 image set. These image sets were independently averaged to create a "mean image." Figure 3.15 shows an example image set and mean image from nadir geometry for the water experiment. The averaging minimizes the temporal effects, namely the thermal eddies.
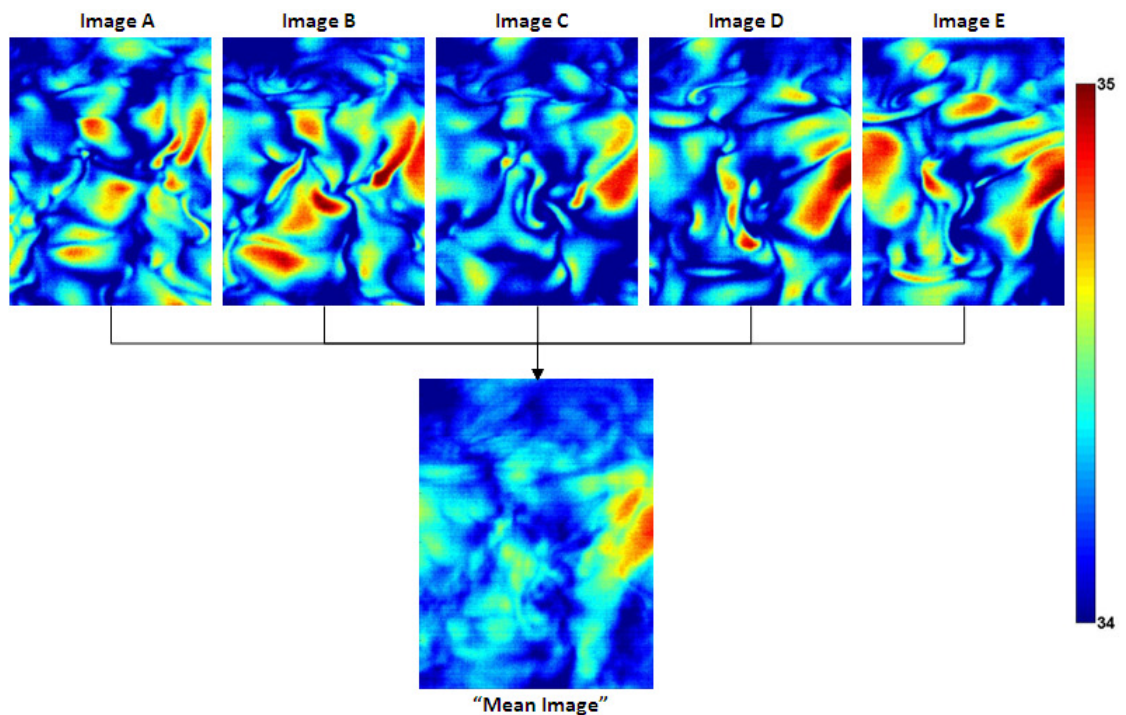
Figure 3.15: Determining the "Mean Image." Temperature in degrees Celsius.

For each "mean image" a ROI was chosen by inspection. The temperature values within the ROI were then averaged in the direction across the

smaller dimension of the flume to create a single array of "mean central pixel temperatures (MCPT)" along the length of the flume, Figure 3.16.
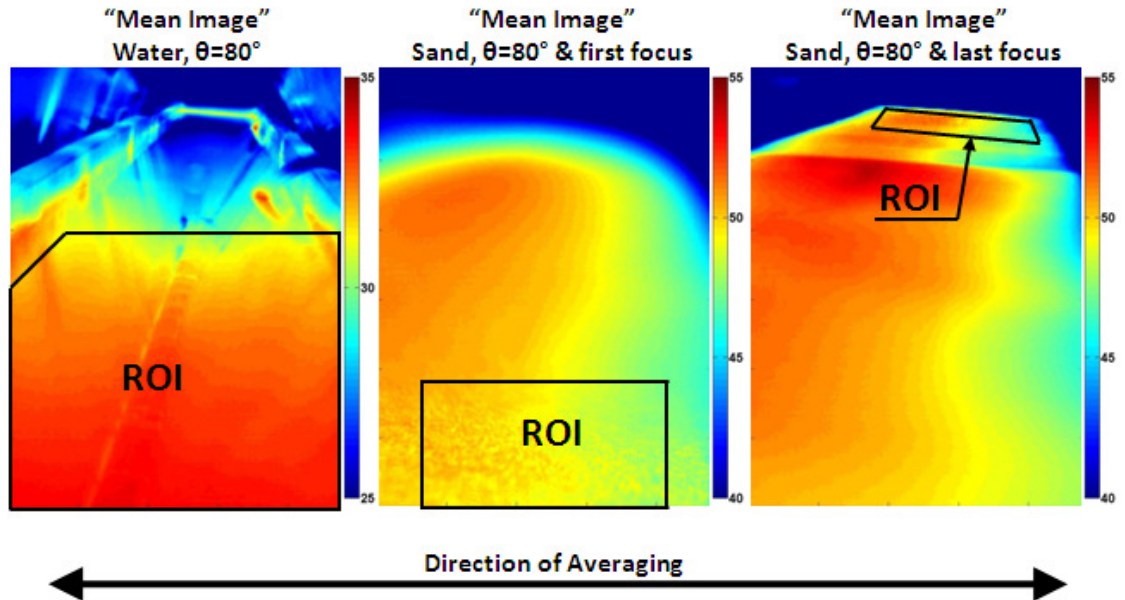
Figure 3.16: Averaging the Regions of Interest. Temperature in degrees Celsius.

The ROI for the "mean image" of the water was chosen to minimize specular reflections from the far end of the flume. The ROI for the "mean images" of the sand were chosen to capture the area in focus and the interior part of the sand surface. The "mean images" of the sand surface show a temperature gradient across the width of the flume with it cooling towards the right. This was caused by the lifting of the insulation to take measurements. The resulting MCPT's were used when plotting the measured temperature values. The data presented later in Figure 3.20 uses the resulting MCPT of the water image in Figure 3.16.

3.6.2 Image Geometry

The experimental setup allowed for the determination of the incident angle associated with each of the pixels in the MCPT. The explanation in this section is for an example MCPT array of six pixels using Figures 3.17, 3.18, and 3.19. Figure 3.17 gives a detailed overview of the situation. Here the instantaneous field of view (IFOV) was defined as

$$\text{IFOV} = \frac{\text{FOV}}{\text{number of pixels in the array}} \tag{3.1}$$

Figure 3.18 shows how the pivot point of the goniometer was dealt with and where the calculations began. The height from the pivot to the surface (H_p), focal distance (L_F), and goniometer arm length (L_G) were measured values. Using these values the others were obtained as follows

$$L_E = \frac{H_p}{\cos(\theta)} \tag{3.2}$$

$$L_T = L_G + L_E \tag{3.3}$$

$$\theta_{B0} = 180° - (90° - \theta) - \frac{\text{FOV}}{2} \tag{3.4}$$

$$L_{rp0} = \sin(90° - \theta) * \frac{L_T + L_F}{\sin(\theta_{B0})} \tag{3.5}$$

Equation 3.5 above applies the Law of Sines to the triangle formed by the ray projected through the lens center to the target and the ray bounding the bottom of the FOV. Figure 3.19 diagrams the pixel incident angles. All the angles and lengths for each IFOV triangle were determined using a pattern, except for the first triangle which was IFOV/2. The values were determined from the following equations, where j is some number in the array of pixels.

$$\theta_{B1} = \theta_{B0} + \frac{\text{IFOV}}{2} \tag{3.6}$$

$$\theta_{Bj} = \theta_{B(j-1)} + IFOV \qquad\qquad (3.7)$$

$$\theta_{Ij} = \theta_{Bj} - 90° \qquad\qquad (3.8)$$

$$L_{rp1} = \sin(\theta_{B0}) * \frac{L_{rp0}}{\sin\left(180° - \frac{IFOV}{2} - \theta_{B0}\right)} \qquad\qquad (3.9)$$

$$L_{rpj} = \sin\left(\theta_{B(j-1)}\right) * \frac{L_{rp(j-1)}}{\sin\left(180° - IFOV - \theta_{B(j-1)}\right)} \qquad\qquad (3.10)$$

By repeating this process for all observation angles overlapping and redundancy

occurred in the measured data. This is because the incident angle of a pixel in one

MCPT array may have matched the incident angle of a different pixel in the following

MCPT array. Recalling that the significant FOV of the FLIR was 19° meant that we

had ±9.5° variation across the pixels. However, this range was lowered for the MCPT

by the selection of the ROI. Other parameters, such as the distance between pixel

incident angles, can be determined by using the Law of Sines on the IFOV triangle

and using the values already obtained. It is further possible to determine the real

world location of each incident angle by using simple geometry to relate all

dimensions to the pivot point.
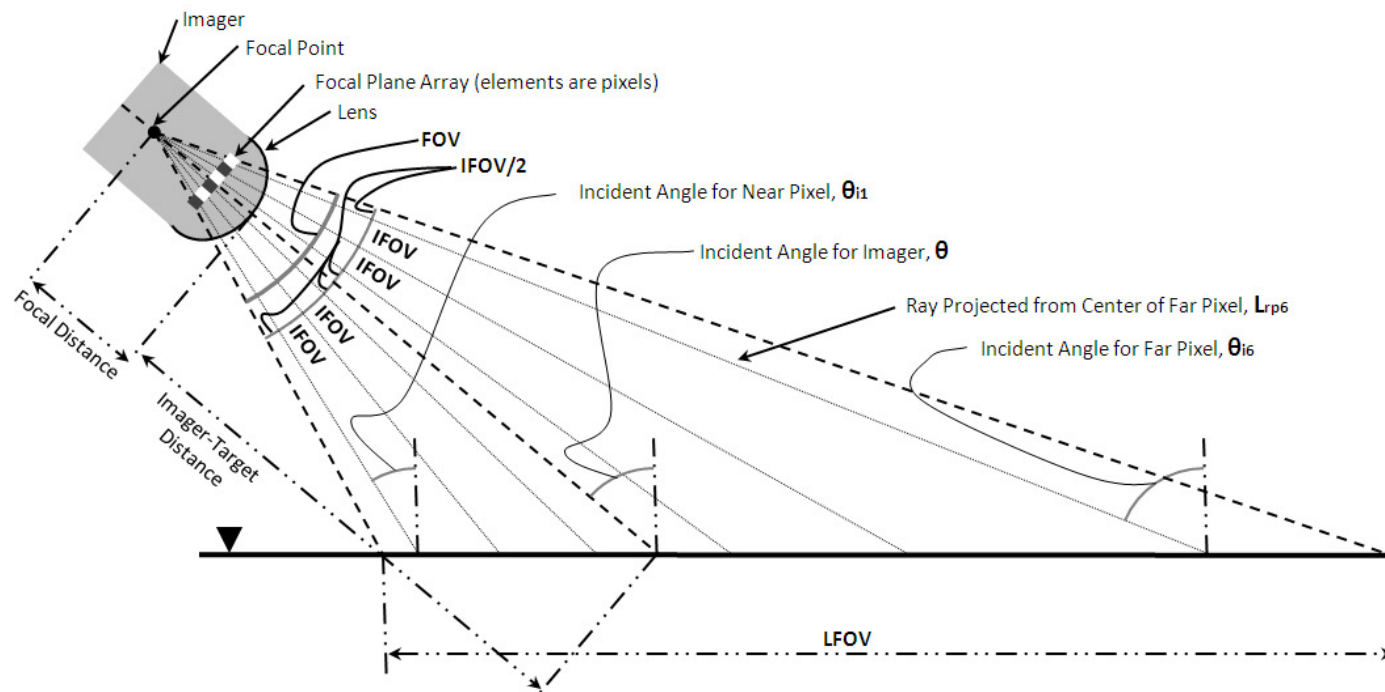
Figure 3.17: Angular Imaging Diagram
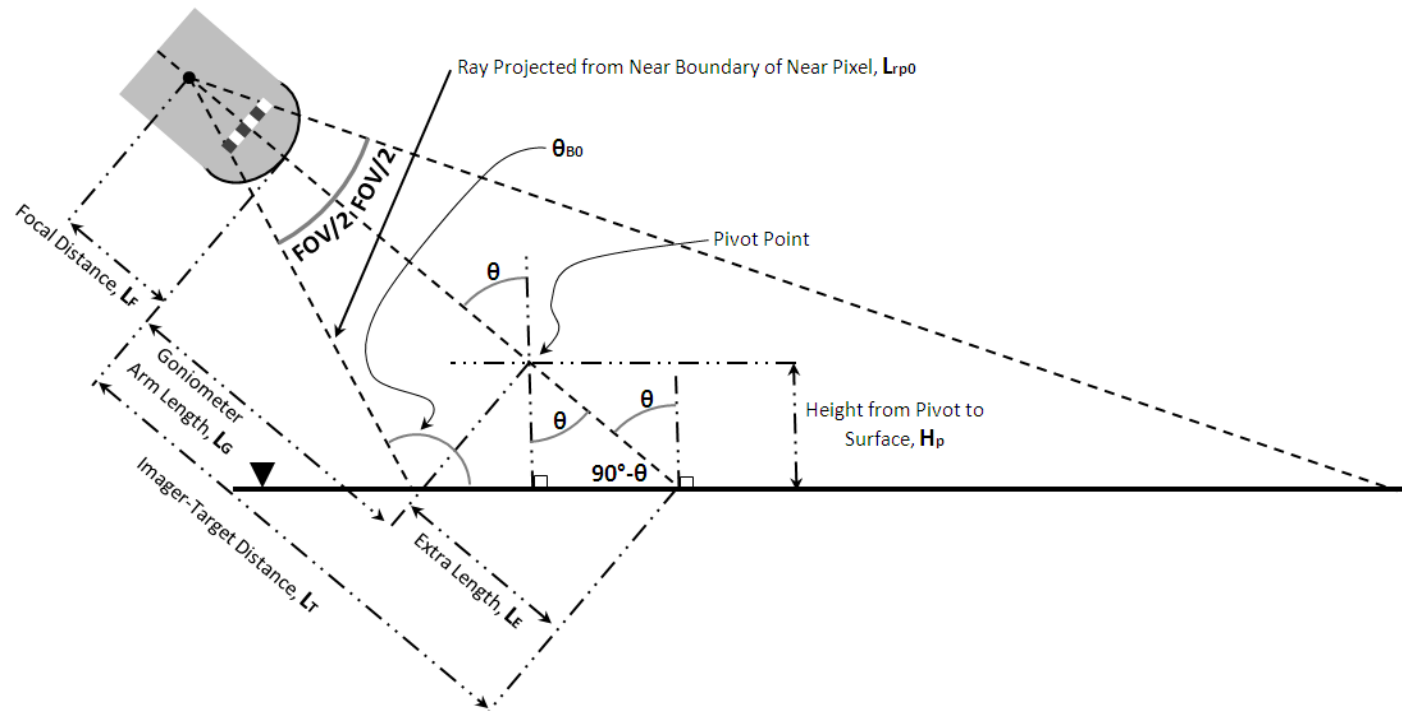
Figure 3.18: Dealing with the Pivot Point
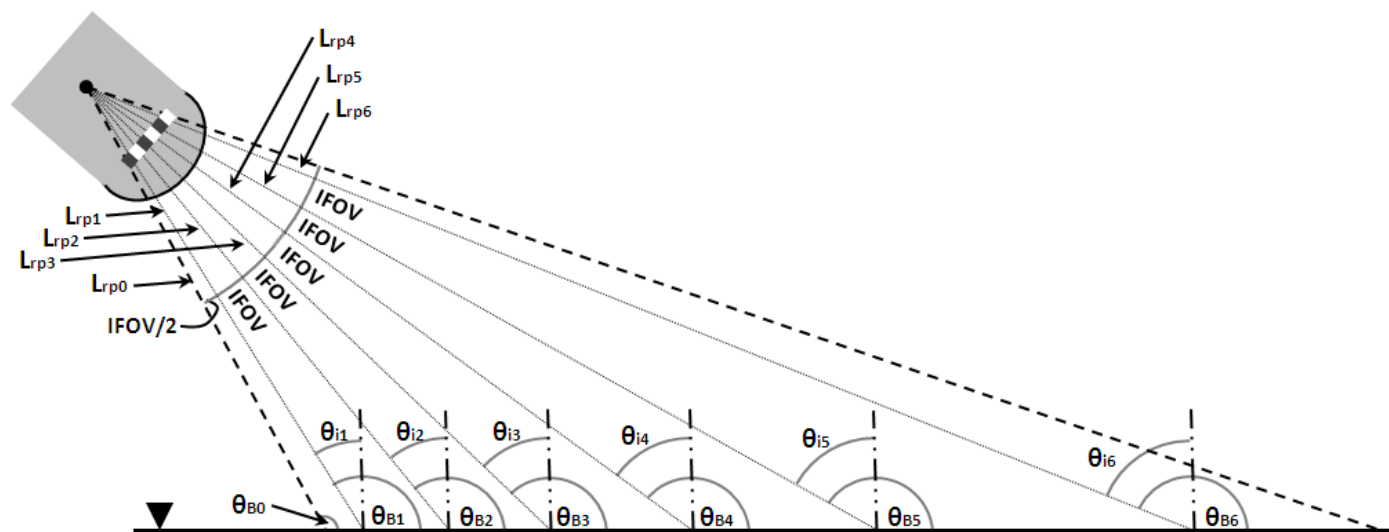
Figure 3.19: Pixel Incident Angle

3.6.3 Example

The MCPT of the water in Figure 3.16 were plotted against the associated pixel incident angles, Figure 3.20. The pixel incident angles were calculated using the methodology in Section 3.6.2.
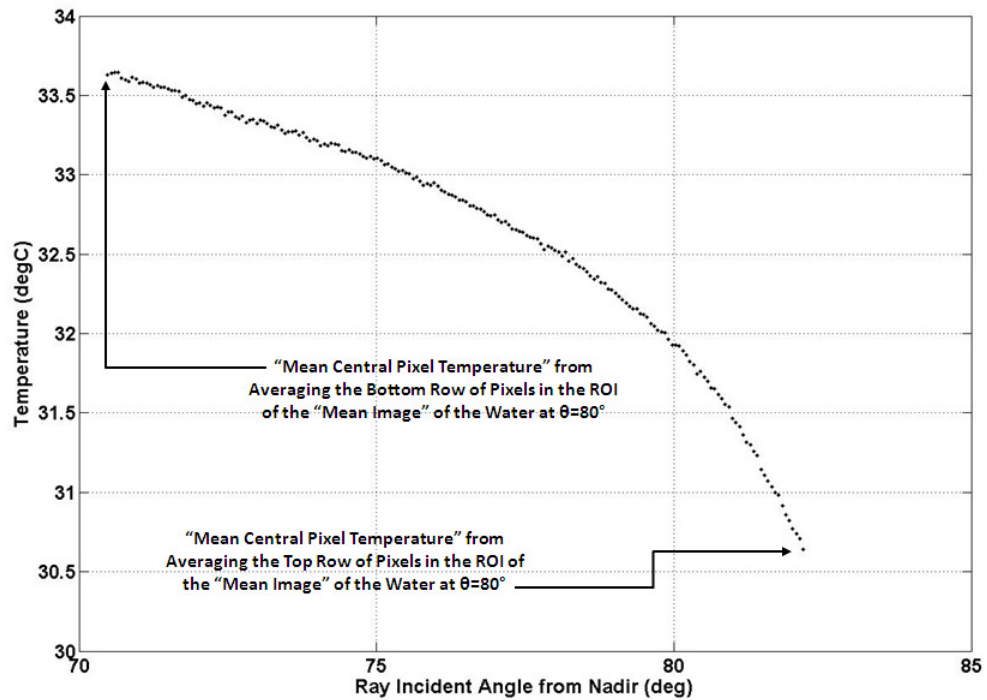
Figure 3.20: FLIR Measurement Results for the Water Experiment at an Observation Angle of 80° from Nadir

The data presented in Figure 3.20 display the expected trend of decreasing temperature with increasing incident angle. This can be further confirmed by observing how the temperature changes in the vertical direction of the "mean image" of the water in Figure 3.16.

Chapter 4

RESULTS

Using the measurements and methodology presented in Chapter 3, it was possible to obtain all the parameters required for performing the calculations, described in Chapter 2, for individual pixels. This chapter reviews the results of that analysis.

4.1   Water Experiment

The MCPT obtained for the water experiment are in Figure 4.1.
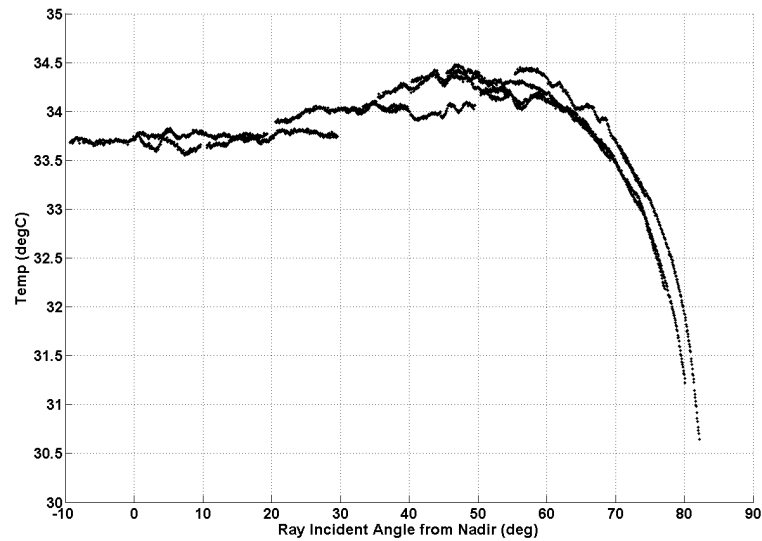
Figure 4.1:   Water Experiment Measured Data

The trend of decreasing measured MCPT (T_θ^M) with increasing angle (θ) is as expected.

4.2   Sand Experiment

The MCPT obtained for the sand experiment are in Figure 4.2.
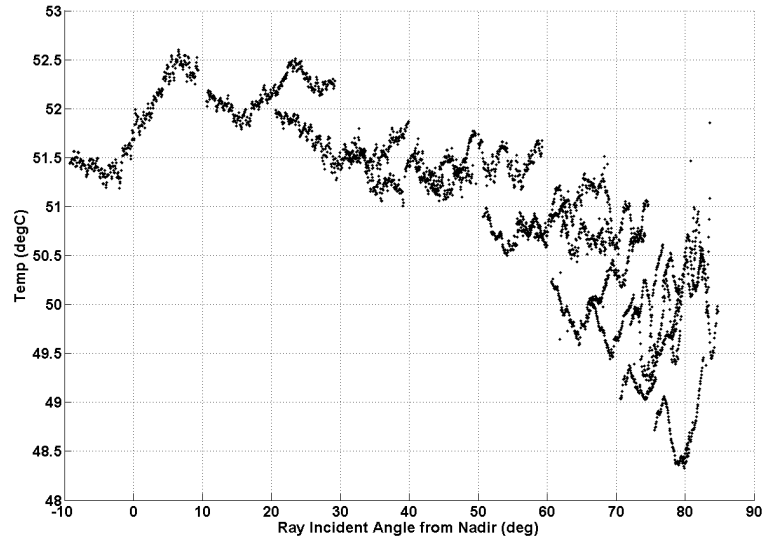
Figure 4.2:   Initial Sand Experiment Measured Data

The significant variability in T_θ^M is concealing the angular trend and is due to the inhomogeneous heating of the heat blankets. To remove this noise T_θ^M was recalculated using only the nearest 80 pixels, Figure 4.3. Throughout the experiment these pixels were capturing the radiant temperature of the material nearest to the FLIR. Furthermore, the distance is smaller between the intersection angles of the rays projected from these pixels, clarified by Figure 3.19. Therefore the initial pixels of T_θ^M are smaller and in a more consistent location on the "sled" where the heating is

more likely to be homogeneous. Also, the across-flume temperature gradient, discussed earlier, may be affecting the results.
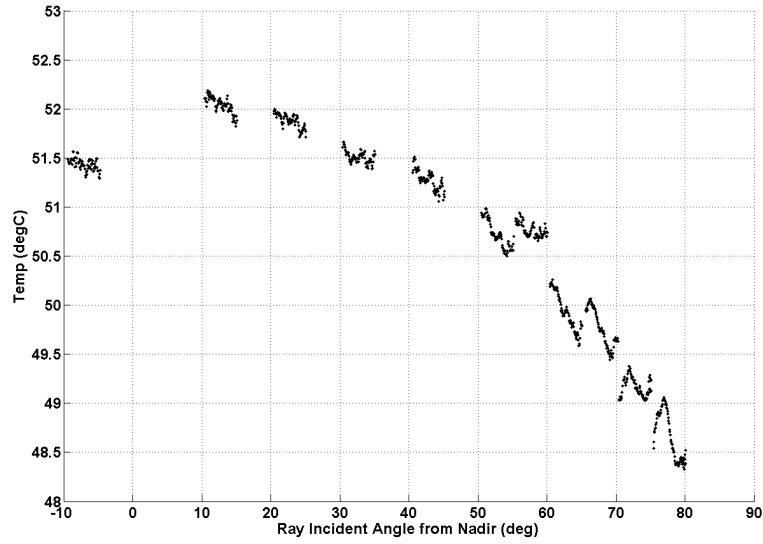
Figure 4.3:   Refined Sand Experiment Measured Data

4.3   Determining Parameters for Calculations

4.3.1   Index of Refraction

Two methods were used to choose index of refraction values. The first method averaged the refractive indices presented by Hale and Querry [1973] for the spectral range of the FLIR (7.5-13μm) and led to a refractive index of 1.2 for the water surface. The data for this method are in Figures 4.4 and 4.5.
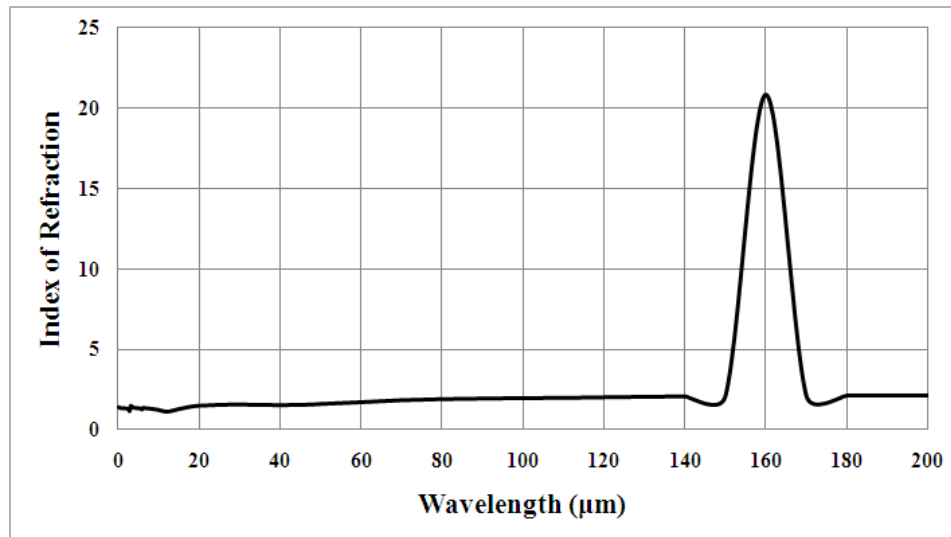
Figure 4.4:   Spectral Refractive Index of Water
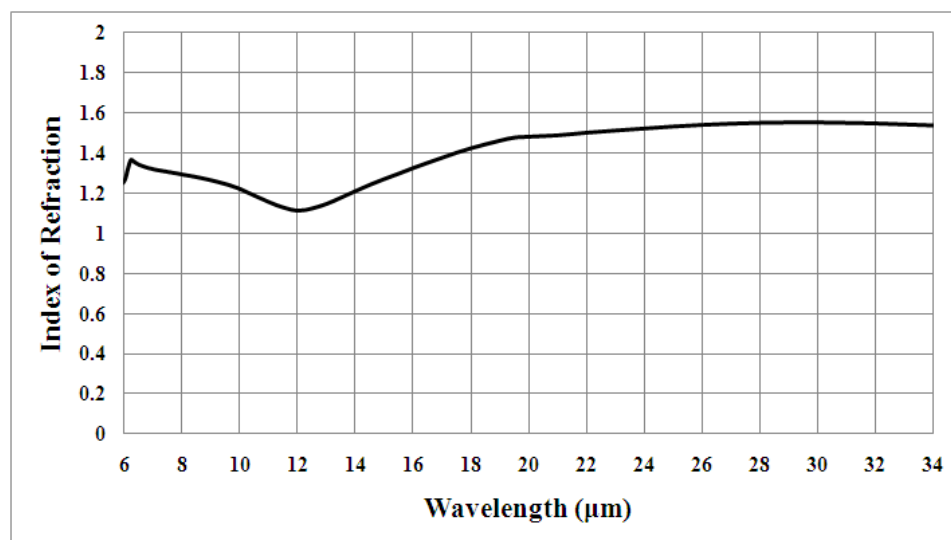
Figure 4.5:   Refined Spectral Refractive Index of Water

The second method ran our prediction using a range of refractive index values. RMS error between the measured and predicted temperatures were obtained and minimized. The results are in Figure 4.6.
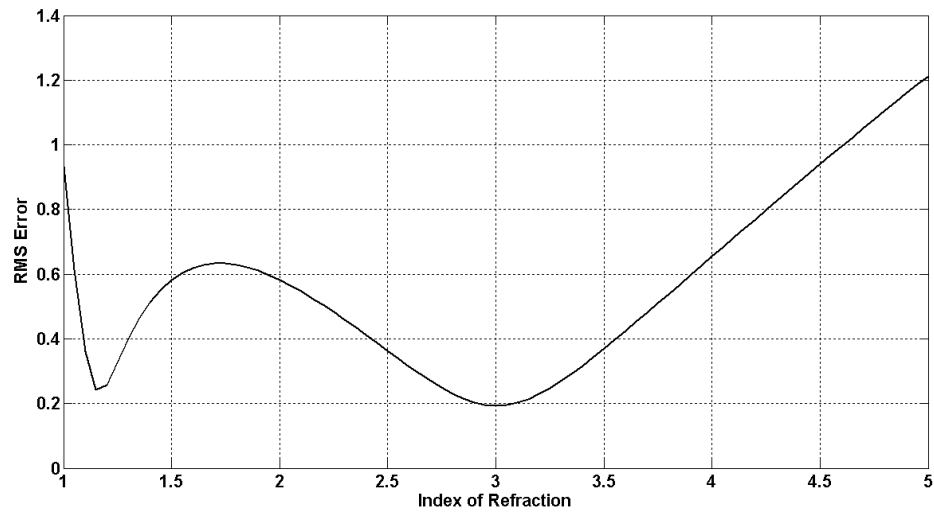
Figure 4.6:   Water Refractive Index from RMS Error

Two minima appear in Figure 4.6 located at 1.16 and 3.00. The three refractive indices were applied to the equations in Chapter 2 and resulted in the angular emissivity shown in Figure 4.7.
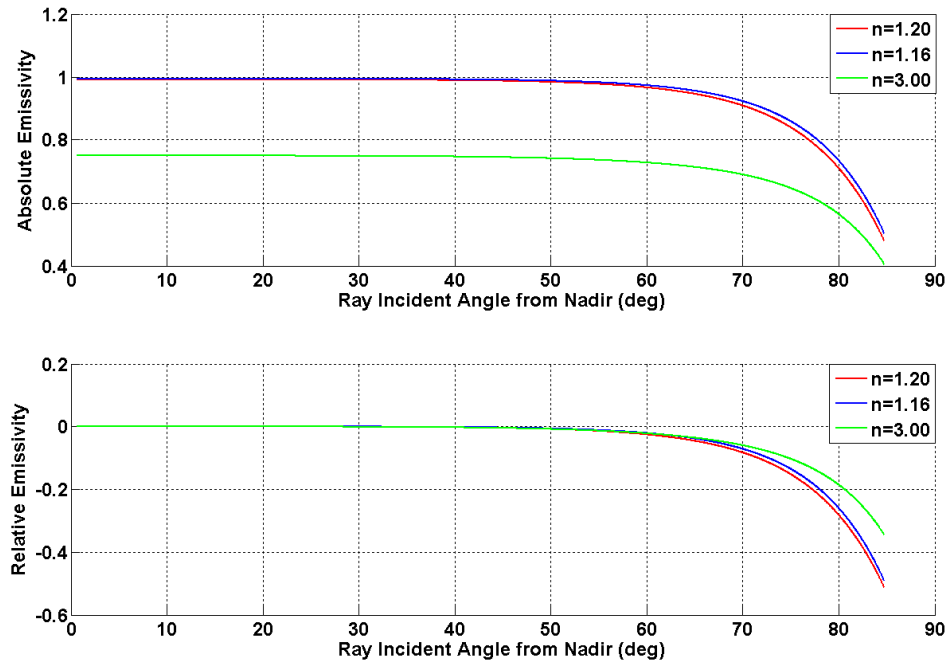
Figure 4.7:   Angular Emissivity of the Water Surface

Weighted averaging the refractive indices presented by Spitzer and Kleinman [1961] for the spectral range of the FLIR led to a refractive index of 1.8 for quartz (n_{quartz}). The data for this method are in Figures 4.8.
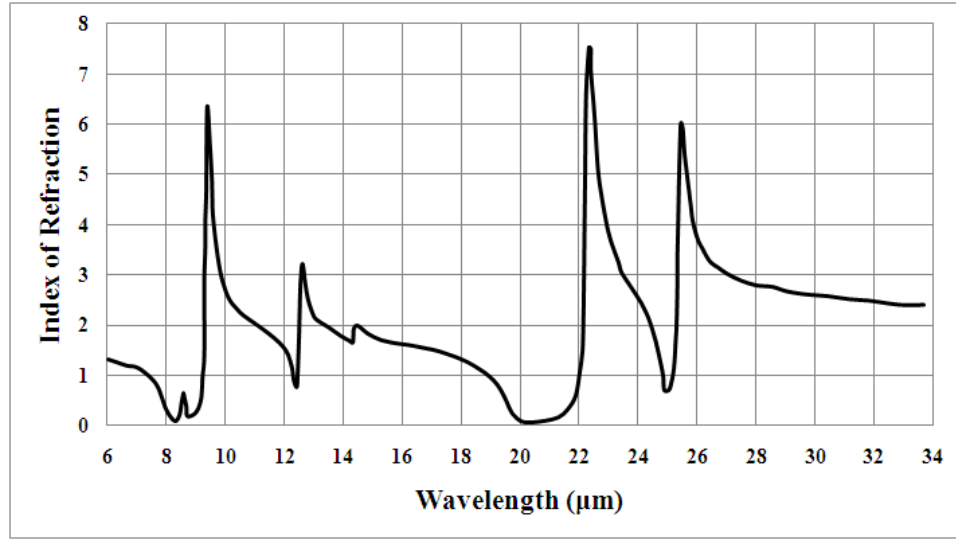
Figure 4.8:   Spectral Refractive Index of Quartz

Using a simple mixing model, Equation 4.1, the refractive index of the sand surface is described

$$n_{sand} = n_{quartz} * (1 - \zeta) + n_{air} * \zeta \ . \tag{4.1}$$

Using a porosity (ζ) of 0.36 and the refractive index of air (n_{air}) of 1 yields a refractive index of 1.5 for the sand surface.

The second method ran our prediction using a range of refractive index values. RMS error between the measured and predicted temperatures were obtained and minimized. The results are in Figure 4.9.
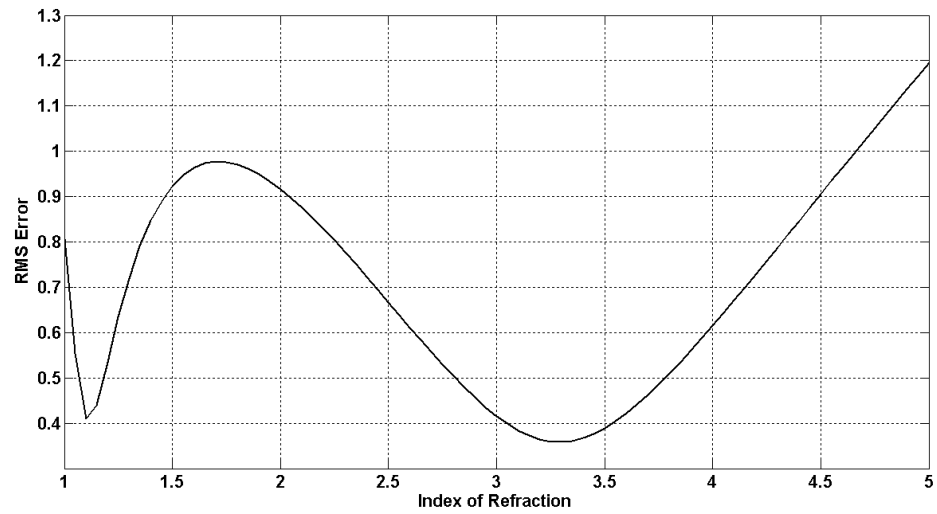
Figure 4.9:   Sand Refractive Index from RMS Error

Two minima appear in Figure 4.9 located at 1.11 and 3.29. The three refractive

indices were applied to the equations in Chapter 2 and resulted in the angular

emissivity shown in Figure 4.10.
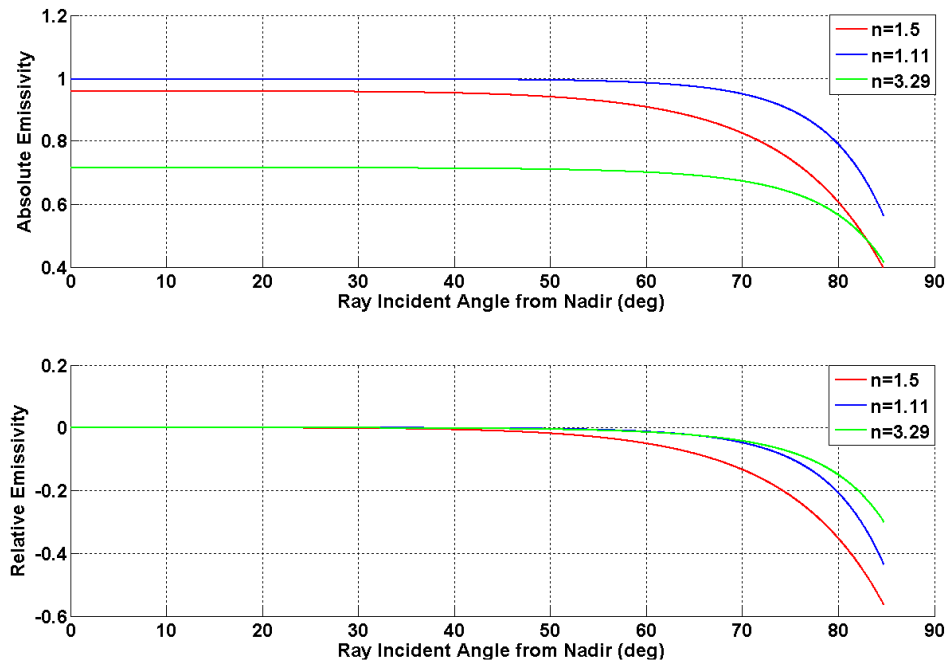
Figure 4.10: Angular Emissivity of the Sand Surface

4.3.2   Reflected Temperature

For both experiments the reflective temperature was chosen as the kinetic air temperature at the time of imagery (Figures III.1 and III.3). There were values for each observation angle.

4.3.3   Object Temperature

The average temperature of the water surface observed near nadir by the IR thermometer was chosen as the object temperature for the water experiment (Figure III.1). There were near nadir IR thermometer values for each FLIR observation angle.

The values of the linear trend, Figure III.2, at the time of imagery were chosen as the object temperatures for the sand experiment. There were values for each observation angle. The linear trend was generated through time using the average of

54

the MCPT for the first three observation angles (0°, 20°, and 30° from nadir) and the last angle (20° from nadir).

4.4   Forward Analysis Results

Results of the forward analysis on the data from the water experiment are presented in Figure 4.11 and 4.12. In Figure 4.11 the colored lines indicate the predicted radiant temperature (T_θ^P) for each ray's incident angle (θ_R) at a specified refractive index. In Figure 4.12 the colored lines indicate the difference between the T_θ^P, for each ray's θ_R, and the object temperature (T_o) at a specified refractive index. Each line connects the data for all the rays associated with a particular image taken at a specific imager incident angle (θ). The black dots indicate the difference between the MCPT (T_θ^M) for each θ_R and T_o.
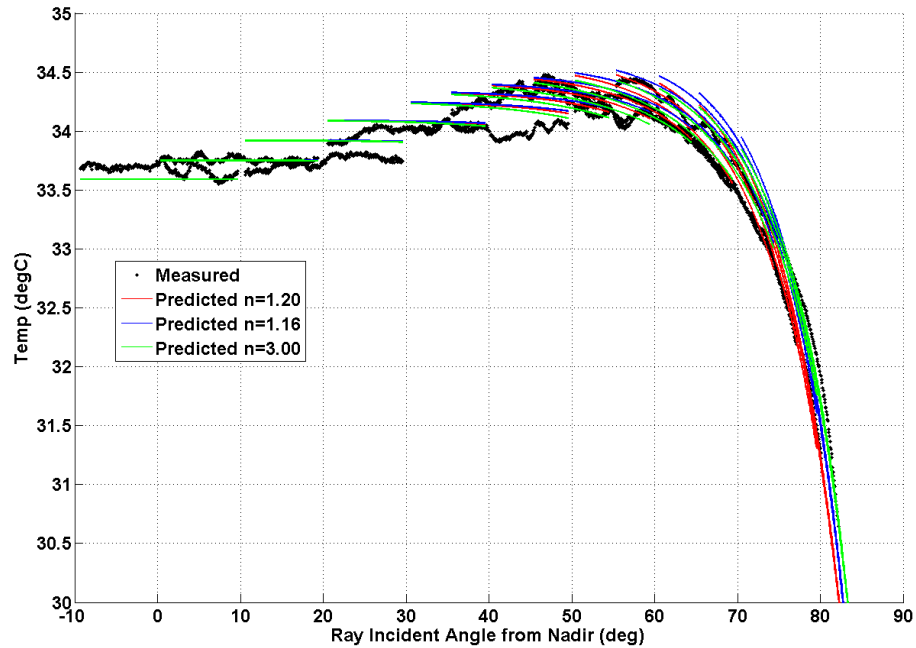
Figure 4.11: Predicted Absolute Temperature Results for Water
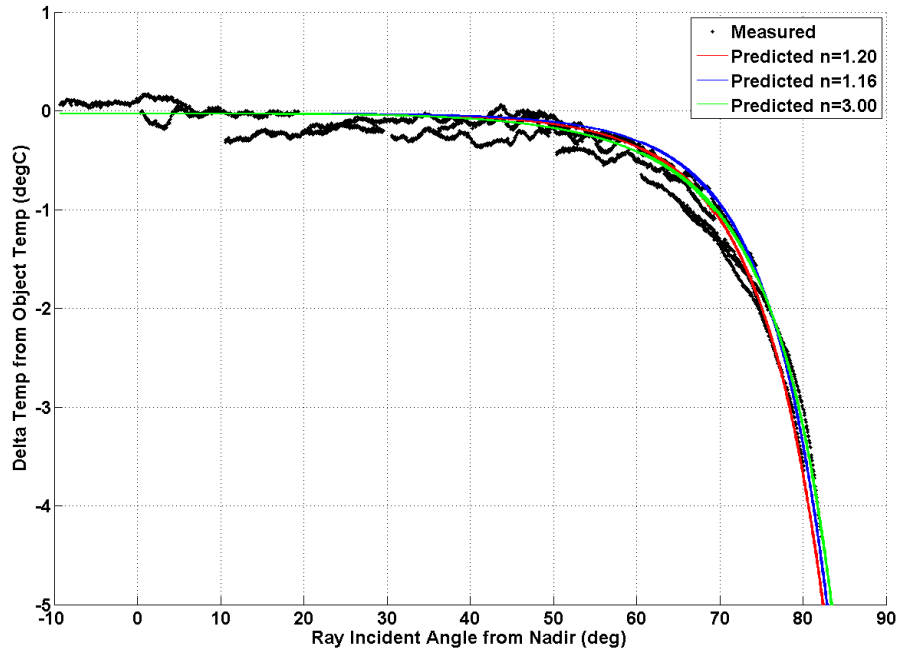
Figure 4.12: Predicted Relative Temperature Results for Water

Index of refraction can have a significant impact on the resulting prediction, however the values chosen appear to graphically fit T_θ^P well with T_θ^M. In Figure 4.11 the temperature raises with angle before it lowers. This trend was caused by the changing T_o and is accounted for within the predictions. Figure 4.12 has a temperature drop of ~4°C at 80°from Nadir compared to T_o. Temperature drops like this can affect the angular GBRS data if unaccounted for. By running the analysis in an inverse method, using T_θ^M to predict T_o, it should be possible to predict the nadir radiant temperature from an angular measurement thus allowing angular images to be transformed by removing the angular effect.

Results of the forward analysis on the data from the sand experiment are presented in Figures 4.13 and 4.14. In Figure 4.13 the colored lines indicate the predicted T_θ^P for each ray's θ_R at a specified refractive index. In Figure 4.14 the

56

colored lines indicate the difference between the T_θ^P, for each ray's θ_R, and the T_o at a specified refractive index. Each line connects the data for all the rays associated with a particular image taken at a specific imager incident angle (θ). The black dots indicate the difference between the MCPT (T_θ^M) for each θ_R and T_o.
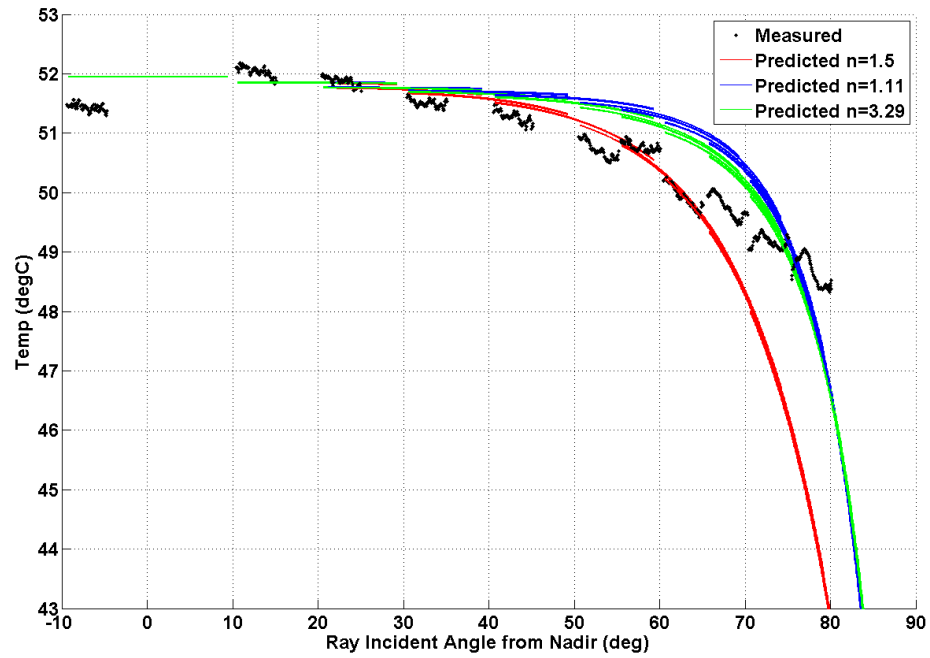
Figure 4.13: Predicted Absolute Temperature Results for Sand
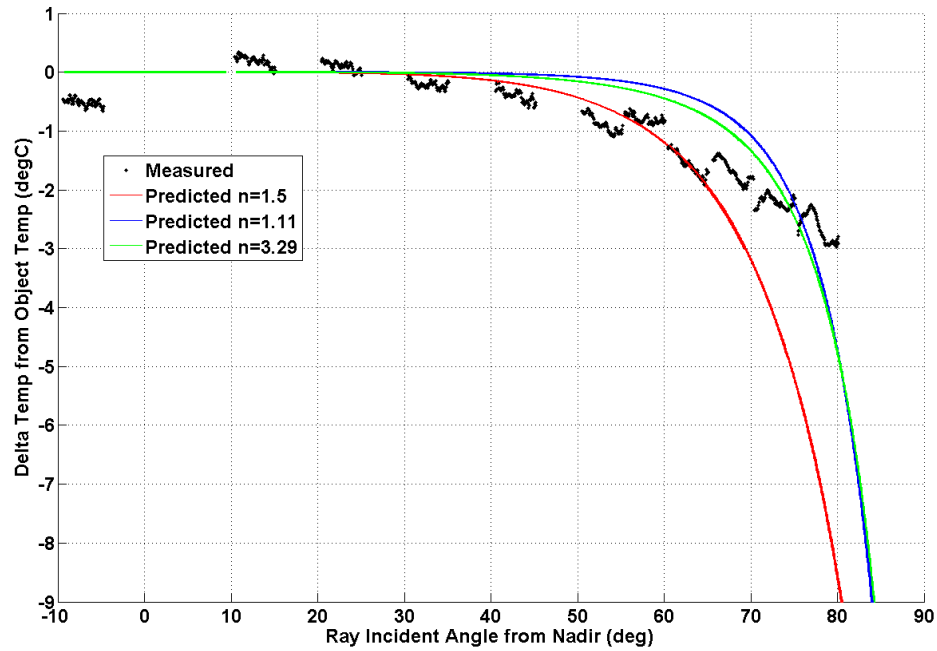
Figure 4.14: Predicted Relative Temperature Results for Sand

Index of refraction can have a significant impact on the resulting prediction. The refractive index of 1.5 graphically fits T_θ^P well with T_θ^M up to about 65° from nadir. Beyond this angle there is growing inaccuracy. The inaccuracy may be attributed to deflection in the goniometer arm. This deflection was not accounted for in the experimental design. However, if the deflection could be quantified it would shift the highly oblique measured values to smaller incident angles and thereby creating a better alignment between the measured and predicted values. Additional inaccuracy may be due to having a granular surface compared to a perfectly flat water surface while another source may be the methodology for choosing a refractive index for sand. The refractive indices of 1.11 and 3.29 graphically appear to contain less error; however the method that chose them brings into to question their physical significance. Figure 4.14 has a temperature drop of ~3°C at 80°from Nadir compared

58

to T_o, similar to the water experiment. Temperature drops like this can affect the angular GBRS data if unaccounted for.

4.5 Transformed Image

Running the analysis presented in Chapter 2 in an inverse method predicted radiant temperature at nadir (T_o^P) for an oblique image were generated, Figures 4.15 and 4.16. The prediction was accomplished in the calculations by using T_θ^M as T_θ and the ambient air temperature as T_P.
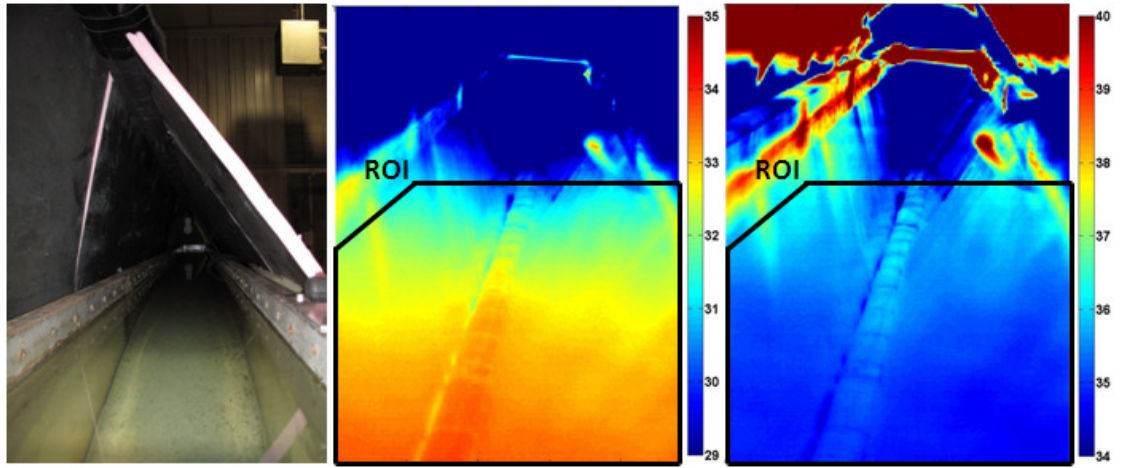
Figure 4.15: Transformed Water Image for θ=80° from Nadir. RGB (left), "Mean Image" (middle), and Transformed Mean Image (right). Temperature in degrees Celsius.

The transformation has had two significant effects in Figure 4.15. The gradient of cooling temperature along the length of the flume was largely removed and the average image temperature was raised. The gradient observed was due to the increasing incident angle for each pixel, clarified in Figure 3.17. The lower average

temperature in the "mean image" was because all the pixels in the image had an oblique incident angle. By transforming all the pixels to their nadir equivalent values the average temperature was raised.

The anomalous structure in the center of the "mean image" running the length of the flume was a specular reflection of the foam pipe insulation covering the metal top bar. The structure could not be removed from the data but did lead to experimental apparatus improvements for the sand experiments.
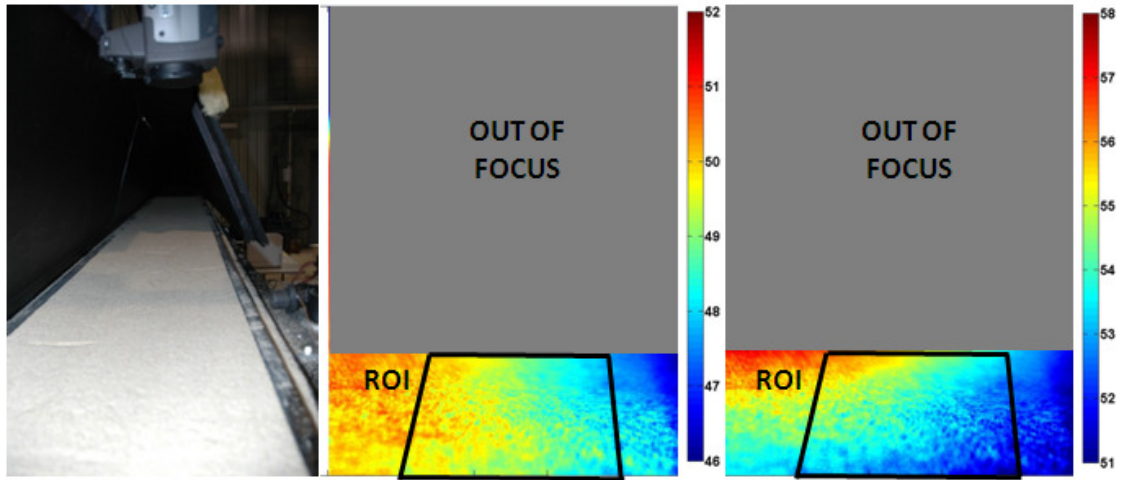
Figure 4.16: Transformed Sand Image for θ=80° from Nadir. RGB (left), "Mean Image" (middle), and Transformed Mean Image (right). Temperature in degrees Celsius.

The transformation of the sand experiment, similar to the water experiment, increased the average temperature of the "mean image" as expected. However, due to the inhomogeneous heating of the sand it was difficult to observe the expected cooling gradient within the image. Furthermore, the horizontal cooling

gradient seen in the "mean image" was caused by the lifting of the insulation to take measurements and could not be removed from the data.

Chapter 5

WOLF RIVER

The previous chapters examined how to accurately capture LST measurements through the use of GBRS. Variations in LST can be used in determining a material's thermal diffusivity. From the thermal diffusivity it may be possible to infer other properties such as lithology, porosity, and moisture content. Field experiments were performed to explore this.

5.1 Data Collection

Data were collected on a sandy beach at a bend of the Wolf River just south of the Cable Bridge Road crossing near Gulfport, Mississippi. The site was located at latitude of +30°29'0.85" and longitude of -89°16'29.03". The FLIR was mounted on a tower which was installed on a sand berm just west of the beach, seen in Figure 5.1. The FLIR overlooked an isolated section of the beach consisting of sand and sandy clay, seen in Figure 5.2. The FLIR was at a height of 5.3m and observed at an angle of 43° from nadir with a 7.3m distance from the lens to the target surface. This observation angle was chosen so that the angular effect of emissivity would not be significant. The FLIR recorded images at 15 minute intervals beginning at 5/26/2010 21:33:00. The image set was culled down to 69 images by removing those containing shadows and people.

Figure 5.2 also calls out two temperature profilers that consisted of an array of Dynamax TM10 temperature sensors collecting data at depths of 3, 5, 7, 10,

15, 20, 25, and 35cm. These depths were chosen to be above the effects of the water table, which was located at ~73cm. Nearby a Hukseflux NR01 four-component net radiation sensor collected radiance measurements. Data were collected autonomously and recorded on a data logger at one minute intervals for just under 30 hours.

Figure 5.1: **Imager Tower Mount.** FLIR was placed on the arm attached to the left tower. The Wolf River can be seen on the left side of the image. The orange flags isolated the section of the beach to be observed.
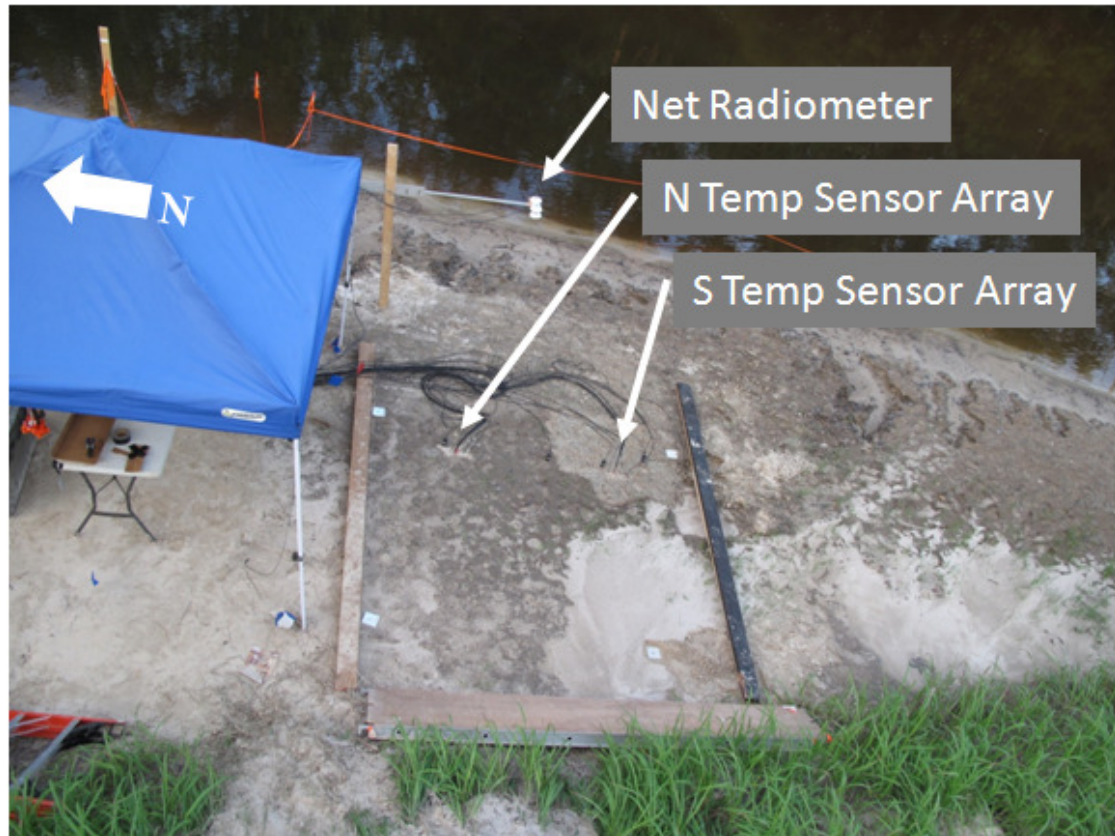
Figure 5.2: **Observation Area.** The Wolf River can be seen on the top of the image. This image was taken from the tower seen in Figure 5.1.

5.2   Measured Data

FLIR images were separated through inspection into three distinct Regions of Interest (ROI) for analysis (Figure 5.3). Two regions were chosen because of their proximity to the kinetic temperature profilers and the third because it was a fresh deposit of sand. Throughout imagery collection the emissivity was set to unity and distance was set to zero for measurement simplicity.
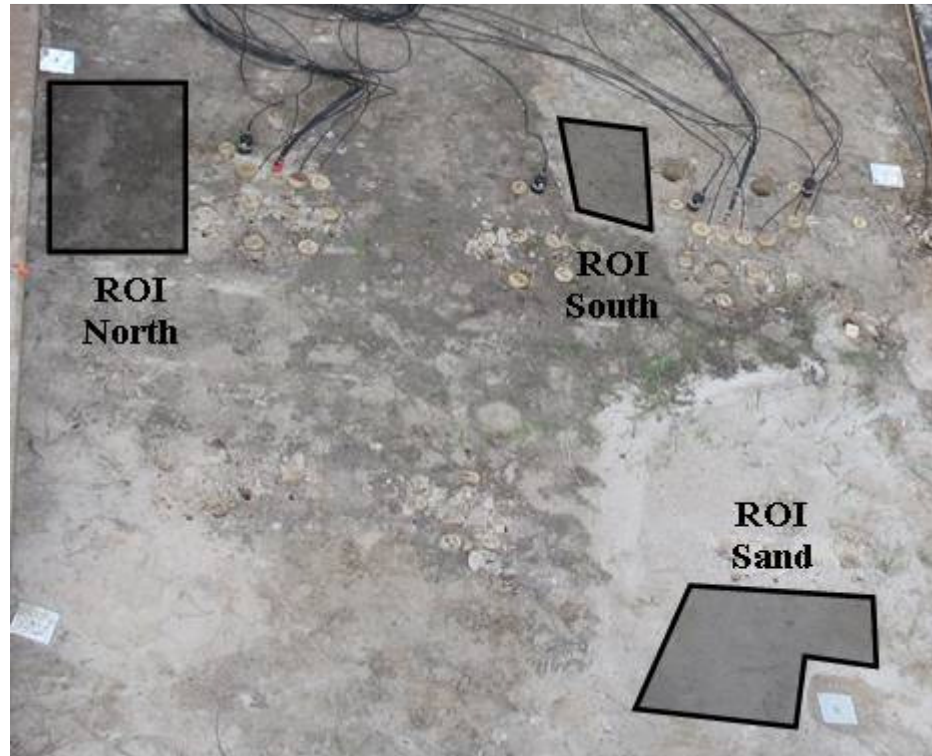
Figure 5.3:   RGB Image of FLIR ROI Used in Analysis

The mean temperature across each ROI was found for each time step. These values were plotted in Figure 5.4 along with the calibrated temperature data from the shallowest temperature sensor (3cm) in each sensor array and the kinetic air temperature. The measured relative humidity data were plotted in Figure 5.5. Incoming, outgoing, and net total data (shortwave and longwave) from the net radiometer were plotted in Figure 5.6.
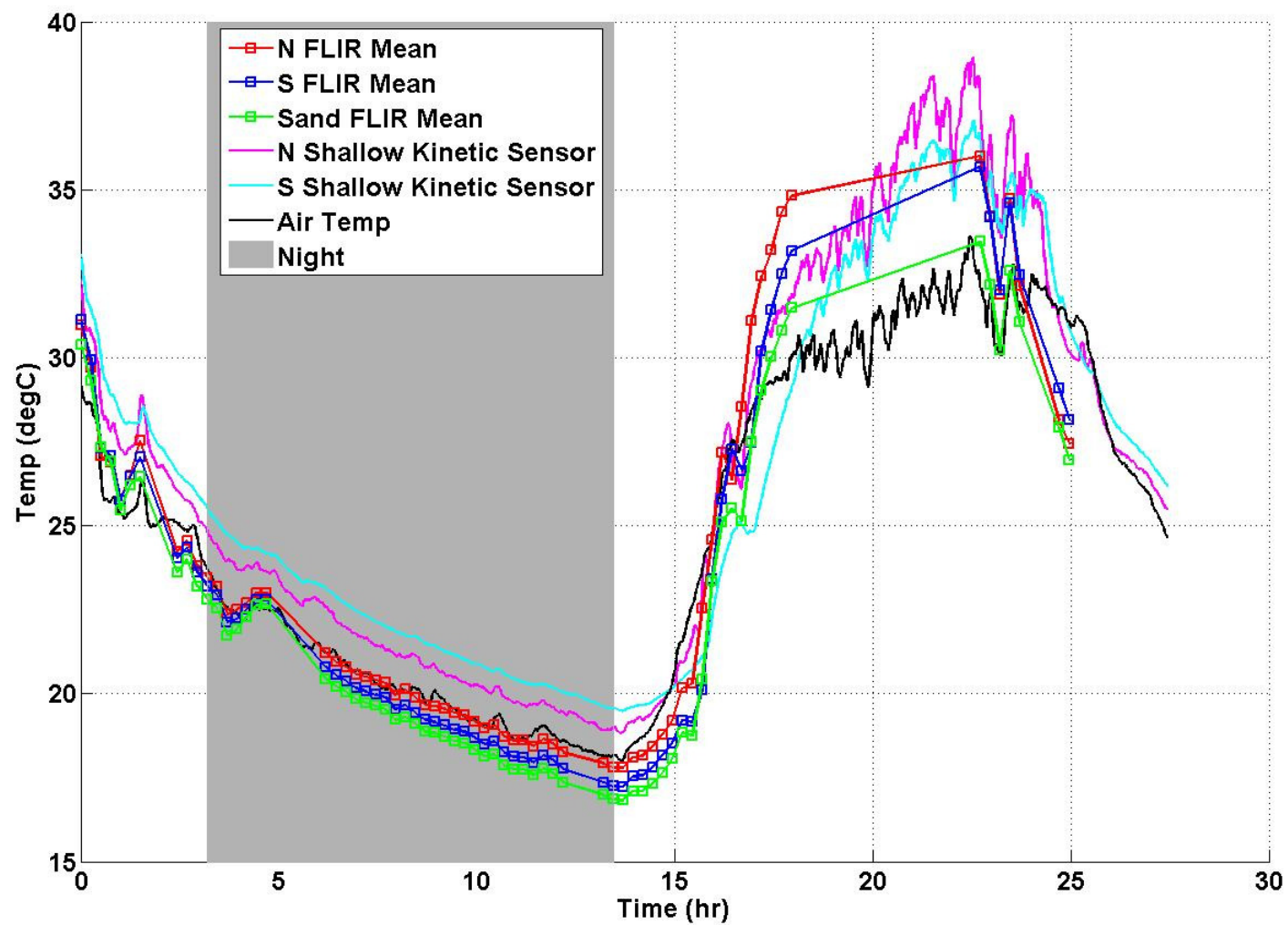
Figure 5.4: **Measured FLIR , Shallow Kinetic Temperature Sensor, and Air Temperature Data.**
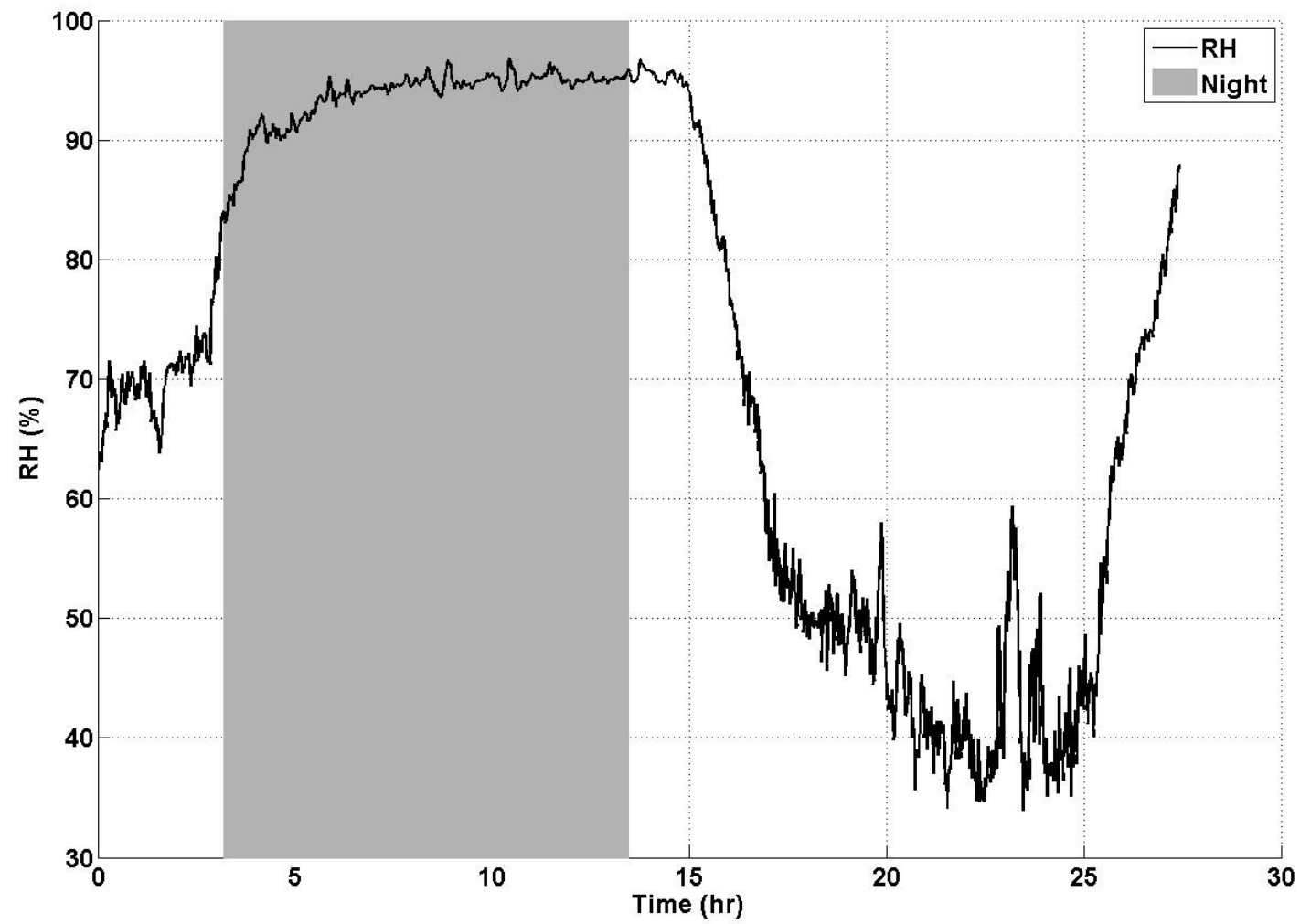
Figure 5.5: Measured Relative Humidity Data
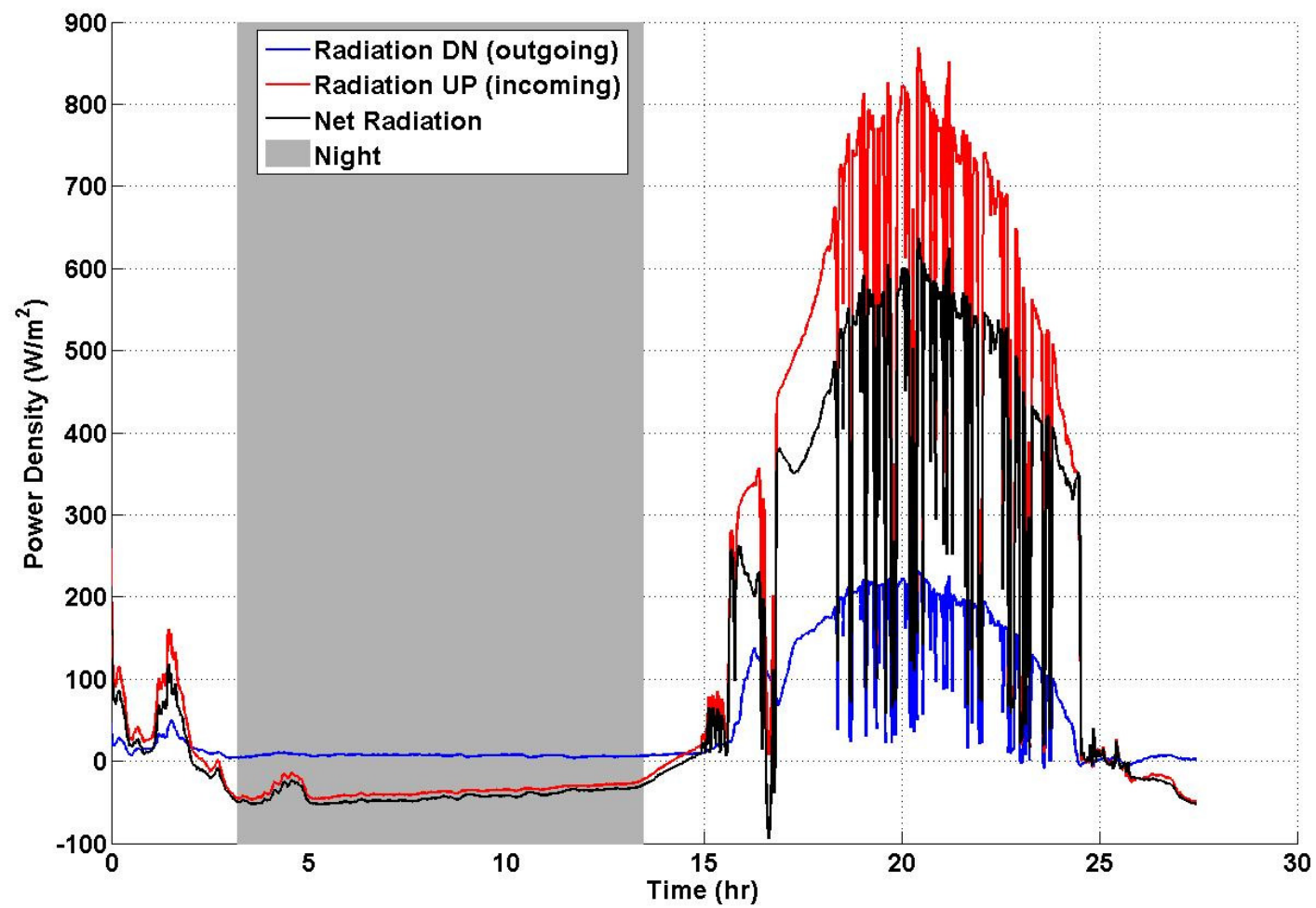
Figure 5.6: Measured Net Radiometer Data.

In Figure 5.4 the variations between the regions are consistent with both the FLIR and kinetic sensor data. However, the kinetic sensor data are offset vertically from the FLIR data. The amplitude or vertical offset is due to blackbody and zero distance assumptions used by the FLIR in its calculation of temperature.

5.3 In Situ Thermal Diffusivity Analysis

Thermal diffusivity ($\acute\alpha$) is a measure of the ability of a substance to transmit a temperature disturbance through a body, and has units of $m^2 s^{-1}$. Thermal diffusivity is defined as:

$$\acute\alpha = \frac{k}{\rho * cp} \tag{5.1}$$

Here, thermal conductivity (k) is the amount of heat energy conducted per unit time, per unit surface area and per unit thermal gradient [W/mK]. Also, specific heat capacity (cp) is the amount of heat required to raise a unit mass of a substance by a unit temperature interval [J/kgK]. Bulk density (ρ) is in units of kg/m^3. Thermal diffusivity derives from the diffusion equation. The one dimensional diffusion equation was defined as (Carslaw and Jaeger, 1959):

$$\acute\alpha * \frac{\partial^2 T}{\partial z^2} = \frac{\partial T}{\partial t} \tag{5.2}$$

where T is temperature, z is depth and t is time. This equation can be used to model the vertical flow of heat in sediment as a function of two variables, depth and time. All models presented below assume a spatially and temporally homogeneous thermal diffusivity. Each in situ method assumed the shallowest temperature sensor was at the surface. This assumption was necessary to carry out the calculations. All temperature sensor depth locations were shifted upward respectively.

5.3.1 Amplitude Method

This method determines diffusivity of the soil given the period and amplitude of surface and subsurface temperature fluctuations. The temperature fluctuation can be described as a cosine wave of the form (Carslaw and Jaeger, 1959):

$$T(z,t) = T_m(z) + T_0 * \exp\left(-z * \sqrt{\frac{\acute{\omega}}{2\acute{\alpha}}}\right) * \cos\left(\acute{\omega}t - z\sqrt{\frac{\acute{\omega}}{2\acute{\alpha}}} - \epsilon\right)$$

(5.3)

Here, the wave form was described by the parameters of the temperature datum (T_m), temperature amplitude (T_0), angular frequency ($\acute{\omega}$), and phase (ϵ). The angular frequency can be described as:

$$\acute{\omega} = \frac{2\pi}{\delta}$$

(5.4)

Where δ is the period and equal to one day. By removing the oscillating term it is possible to quantify the relative damping in terms of amplitude change with depth:

$$\frac{T(z) - T_m(z)}{T_0} = \frac{A(z)}{A_0} = \exp\left(-z * \sqrt{\frac{\acute{\omega}}{2\acute{\alpha}}}\right)$$

(5.5)

Solving for thermal diffusivity is accomplished by inverting the equation.

$$\acute{\alpha} = \frac{\acute{\omega} * Z^2}{2 * \ln\left(\frac{A(z)}{A_0}\right)^2}$$

(5.6)

For the final diffusivity results from this model the temperature amplitudes chosen for the analyses came from the shallowest sensor and the deepest sensor. The thermal diffusivities resulting from the data from these sensors yielded the most reasonable results. Furthermore these sensors allotted the most depth for thermal diffusion to occur.

5.3.2 Numerical Method

For this one-dimensional analysis, thermal diffusivity was solved for using an explicit finite-difference method. First, the derivatives in Equation 5.2 were redefined. The depth derivative was described by a central difference scheme and the time derivative was described by a forward difference scheme.

$$\left(\frac{\partial^2 T}{\partial z^2}\right)_j = \frac{\left(\frac{\partial T}{\partial z}\right)_{j+\frac{1}{2}} - \left(\frac{\partial T}{\partial z}\right)_{j+\frac{1}{2}}}{\Delta z} = \frac{\left(\frac{T_{j+1}-T_j}{\Delta z}\right) - \left(\frac{T_j - T_{j-1}}{\Delta z}\right)}{\Delta z} = \frac{T_{j+1}-2T_j+T_{j-1}}{\Delta z^2} \tag{5.7}$$

$$\left(\frac{\partial T}{\partial t}\right)^n = \frac{T^{n+1}-T^n}{\Delta t} \tag{5.8}$$

Here, j is some depth and n is some time. Substituting Equation 5.7 and Equation 5.8 into Equation 5.2 resulted in:

$$\acute{\alpha}\frac{T_{j+1}^n - 2T_j^n + T_{j-1}^n}{\Delta z^2} = \frac{T_j^{n+1}-T_j^n}{\Delta t} \tag{5.9}$$

or

$$T_j^{n+1} = T_j^n + \frac{\acute{\alpha}*\Delta t}{\Delta z^2}\left(T_{j+1}^n - 2T_j^n + T_{j-1}^n\right) \tag{5.10}$$

Equation 5.10 predicts the temperature for one time step by using only values from the previous time step. A Dirichlet boundary condition was used at the surface along with the shallowest sensor data. A Nuemann boundary condition was used at the depth of the deepest sensor. The resulting modeled temperatures were used along with the original measured temperature data to determine a Root Mean Square (RMS) error.

$$\text{RMS Error} = \sqrt{\frac{\sum\left(\text{Predicted}_j^n - \text{Measured}_j^n\right)^2}{\sum j \sum n}} \tag{5.11}$$

The model repeated this process for multiple guesses of the thermal diffusivity. A value was converged to by minimizing the RMS error.

5.3.3 Double Boundary Value Method

This method numerically solved an analytical solution of the temperature profile through depth and time for a one dimensional semi-infinite medium given thermal diffusivity. Then it converged to a value for thermal diffusivity by comparing the predicted profile with the measured profile and calculating a RMS Error , similar to the numerical method. The temperature profile was predicted by a double boundary value problem. It was solved through substitution as shown in Figure 5.7.
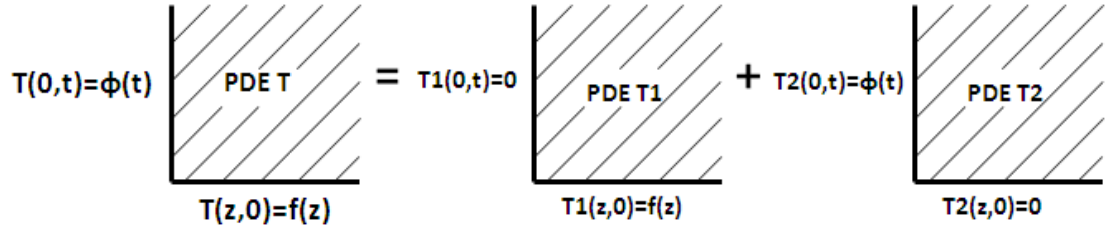
Figure 5.7: Boundary Value Problem for Double BV Method

Here, $\phi(t)$ was the surface temperature profile through time and $f(z)$ is the initial temperature profile through depth. Solving these two boundary value problems resulted in (Carslaw, 1921):

$$T(z,t) = \frac{1}{2\sqrt{\pi \acute{\alpha} t}} \int_0^\infty f(z') \left\{ e^{\frac{-(z-z')^2}{4\acute{\alpha}t}} - e^{\frac{-(z+z')^2}{4\acute{\alpha}t}} \right\} dz'$$

$$+ \frac{z}{2\sqrt{\pi \acute{\alpha}}} \int_0^t \phi(\tau) \left\{ \frac{e^{\left(\frac{-z^2}{4\acute{\alpha}(t-\tau)}\right)}}{(t-\tau)^{\frac{3}{2}}} \right\} d\tau$$

$$(5.12)$$

Both φ(*t*) and the f(*z*) functions describe the fluctuations from the initial surface temperature. So, the measured temperature data were altered to a "normalized" temperature by subtracting off the measured, initial surface temperature. The φ(*t*) function was created by fitting a cubic spline to the "normalized" surface temperature data, assumed to be the shallowest kinetic sensor data. The f(*z*) function was defined in two parts. For the surface to the deepest measurement it was defined by fitting a cubic spline to the "normalized" initial temperatures of each kinetic temperature sensor. From the deepest measurement to a depth of infinity it was defined as a sigmoidal decay back to zero. Approaching zero as depth goes to infinity is an assumption of the analytical solution and required for it to be solved. The sigmoidal shape was chosen because of its natural appearance. Figures 5.8 and 5.9 show the chosen f(*z*) and φ(*t*) functions with the measured data for a graphical fit.
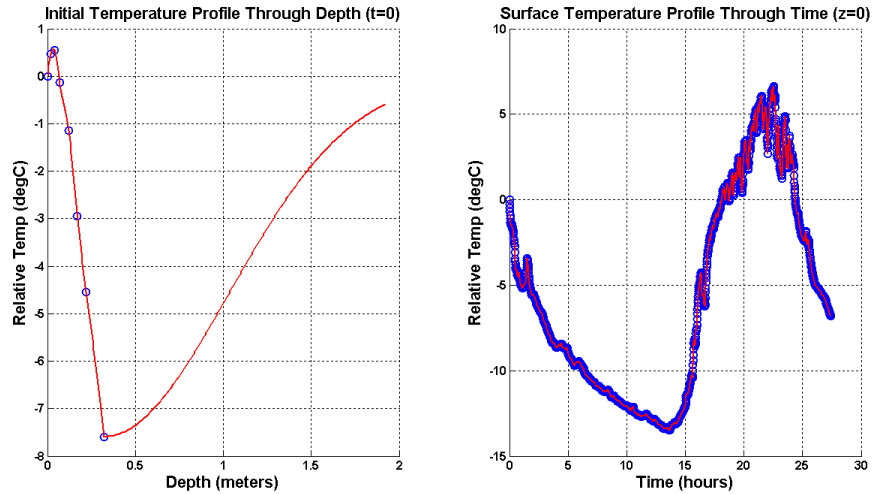
Figure 5.8: Northern Profile Boundary Functions
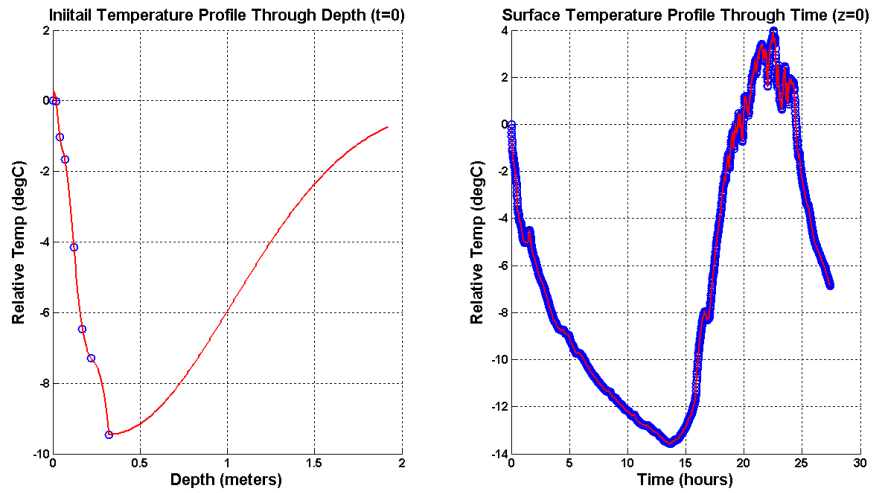
Figure 5.9:   Southern Profile Boundary Functions

Predicted temperatures were obtained by solving Equation 5.12 and adding in the measured, initial surface temperature. RMS error was then obtained using Equation 5.11. The model repeated this process for multiple guesses of the thermal diffusivity. A value was converged to by minimizing the RMS error.

5.3.4   Results

The Numerical and Double BV methods converged to thermal diffusivity values by minimizing RMS error, Figure 5.10.   The values of thermal diffusivity from the three in situ analysis methods on the two temperature profiles are presented in Table 5.1.
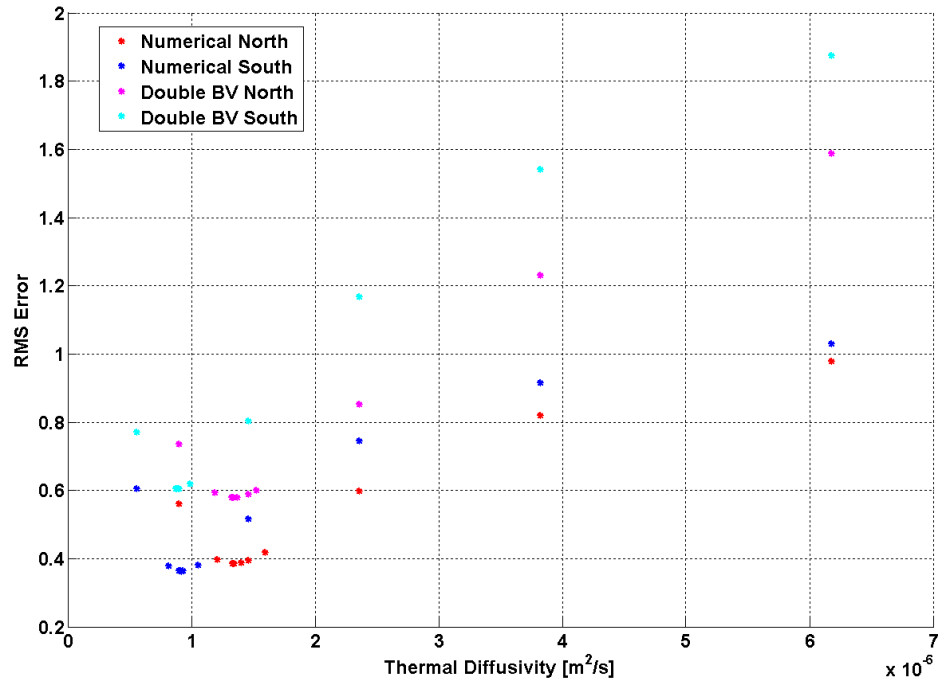
Figure 5.10: RMS Error Minimization

Table 5.1: In Situ Diffusivity Results

	Amplitude	Numerical	Double BV
ά(North) [m^2/s]	0.7094e-6	1.3384e-6	1.3291e-6
ά(South) [m^2/s]	0.6478e-6	9.1877e-7	8.7696e-7

Typical diffusivity values reported in the literature are ~2.5e-7 m^2/s for dry sand and ~9.2e-7 m^2/s for wet sand. Volumetric soil moisture content measured at the site was approximately 16 % and 32% at the north and south profiles, respectively. The Numerical and Double BV results were consistently near the typical value for wet sand. This was an indication of good model accuracies.

These thermal diffusivity values were then used to run the models in a forward scheme that predicted the temperature through depth and time. This predicted

75

temperature was then compared with the measured data for the Northern profile,
Figure 5.11, and the Southern profile, Figure 5.12.
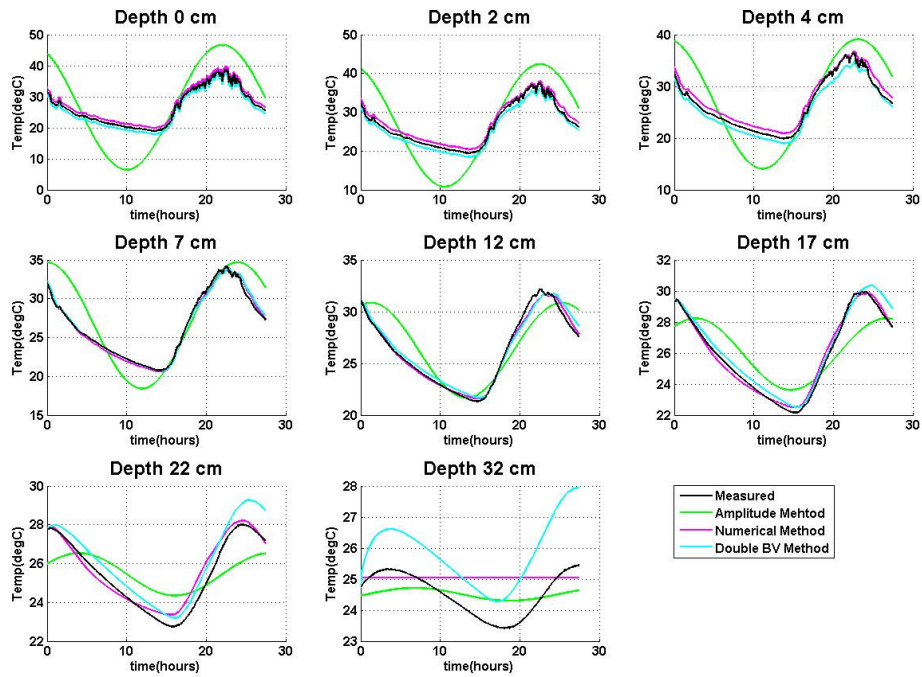
Figure 5.11: Northern Profile Results
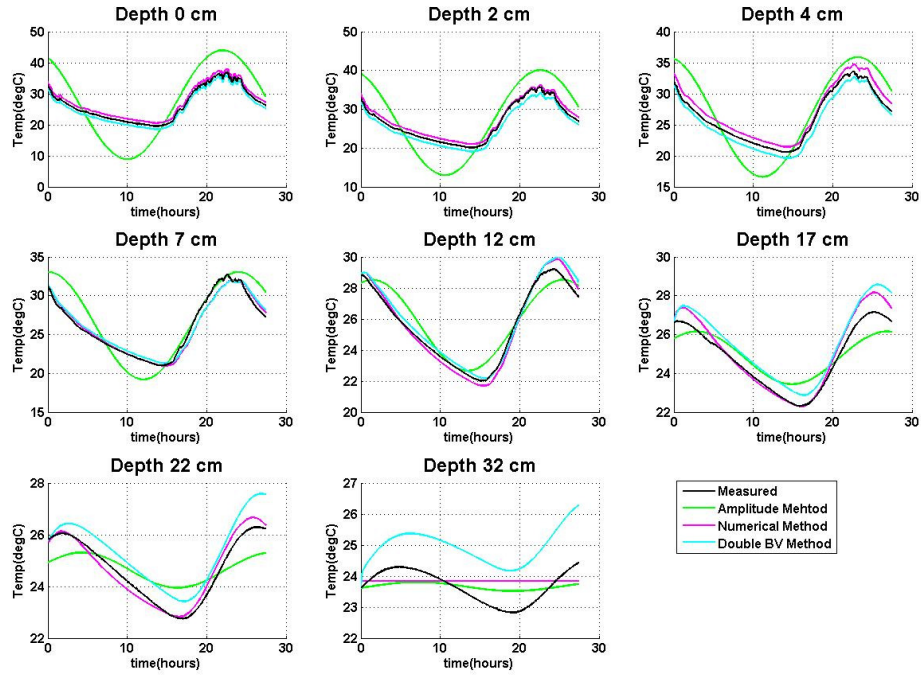
Figure 5.12: Southern Profile Results

Figure 5.11 and Figure 5.12 give a graphical fit of the in situ diffusivity analysis methods to the measured data. It is important to note that the temperature scales are variable in both Figures 5.11 and 5.12. The analysis assumed the shallowest temperature sensor was at the surface. This assumption was necessary to carry out the calculations. All temperature sensor depth locations were shifted upward respectively. The first three subplots in each figure shifted the data from the Numerical and Double BV methods by 1° to minimize plotting overlap. In the first subplot the measured, Numerical, and Double BV lie directly on top of each other, because the measured data were the surface boundary conditions for the Numerical and Double BV methods. The first data point of the Double BV method on every subplot lies directly on top of the measured data, because of the Double BV method's initial temperature profile

77

boundary condition. The final subplot in each figure has a horizontal line for the

Numerical method due to the Nuemann boundary condition.

5.4 Remote Diffusivity Analysis

5.4.1 Theory

Carslaw and Jaeger [1959] defined the solution for a semi-infinite solid

with zero initial temperature and a constant surface heat flow density as:

$$T(z, t) = \frac{2F_0}{k} \left\{ \left(\frac{\acute{\alpha}t}{\pi} \right)^{\frac{1}{2}} e^{-\frac{z^2}{4\acute{\alpha}t}} - \frac{z}{2} \text{erfc} \left(\frac{z}{2\sqrt{\acute{\alpha}t}} \right) \right\} \tag{5.13}$$

The cooling of the earth's surface on a clear, windless night can be approximated by

the removal of heat at a constant heat flow density from a semi-infinite medium as

expressed in Equation 5.13. The surface temperature $(z=0)$ is:

$$T(0, t) = \frac{2F_0}{k} \left(\frac{\acute{\alpha}t}{\pi} \right)^{\frac{1}{2}} \tag{5.14}$$

or

$$T(0, t) = \left(\frac{2F_0\sqrt{\acute{\alpha}}}{k\sqrt{\pi}} \right) \sqrt{t} \tag{5.15}$$

with F_0 being the constant heat flow density $[Wm^{-2}]$. Equation 5.15 can be inverted

to solve for thermal diffusivity:

$$\acute{\alpha} = \left[\frac{k\sqrt{\pi}}{2F_0} \left(\frac{T(0,t)}{\sqrt{t}} \right) \right]^2 \tag{5.16}$$

From here, the thermal effusivity $[Ws^{1/2}m^{-2}K^{-1}]$ can also be determined:

$$\text{Thermal Effusivity} = \sqrt{\frac{k\rho}{c_p}} = \sqrt{\frac{k^2}{\acute{\alpha}}} = \frac{2F_0}{\sqrt{\pi} \left(\frac{T(0,t)}{\sqrt{t}} \right)} \tag{5.17}$$

78

5.4.2 Analysis

Dividing the experiment into two increments (night and morning) where the net radiometer readings are relatively stable (Figure 5.6) allows F_0 to be estimated as the average value across the time increment. The values obtained were listed in Table 5.2.

The average temperature across an ROI was determined through time and with respect to the average ROI temperature at the increment start time. This average temperature time series was plotted versus the square root of the elapsed time. A linear trend was fit to the data on the plot and slope was obtained. Since $T(0, t) = slope * \sqrt{t}$ (Equation 5.15), the slope can be used in place of $T(0, t)/\sqrt{t}$ when calculating thermal diffusivity and thermal effusivity. Plots for the night increment are shown in Figure 5.13 and for the morning increment in Figure 5.14. The resulting slope values are listed in Table 5.2.
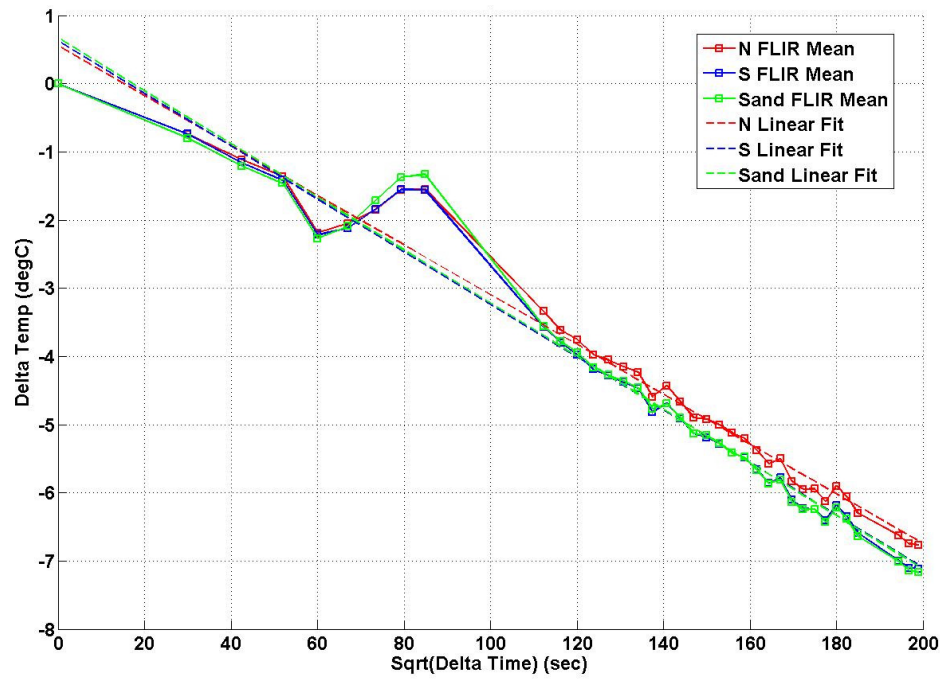
Figure 5.13: Night Linear Plot
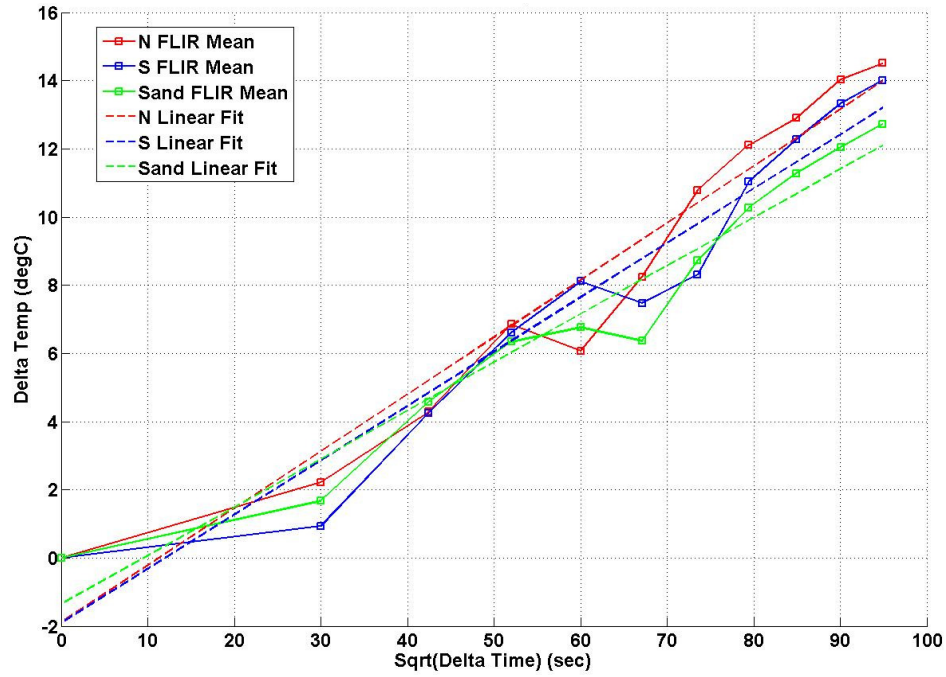
Figure 5.14: Morning Linear Plot

Table 5.2:   Remote Analysis Values

	Night	Morning
Start Time	5/27/2010 00:14:00	5/27/2010 12:59:00
End Time	5/27/2010 11:16:00	5/27/2010 15:31:00
Relative Start Time [hours]	2.67	15.42
Relative End Time [hours]	13.71	17.96
Mean F_0 $[W/m^2]$	-41.71	241.17
North ROI Linear Fit Slope	-0.0365	0.1672
South ROI Linear Fit Slope	-0.0386	0.1593
Sand ROI Linear Fit Slope	-0.0389	0.1417

The cored samples of the site soils remain sealed and have yet to be analyzed, because of this the soils' thermal conductivities are unknown. A value of 1.5 $[Wm^{-1}K^{-1}]$ was assumed for each ROI.

5.4.3 Results

Thermal diffusivity and thermal effusivity values were calculated using Equations 5.16 and 5.17 and the values from Table 5.2.

Table 5.3:   Remote Results

	Night	**Morning**
ȧ(North ROI) $[m^2/s]$	1.353e-6	0.850e-6
ȧ(South ROI) $[m^2/s]$	1.517e-6	0.771e-6
ȧ(Sand ROI) $[m^2/s]$	1.541e-6	0.610e-6
North ROI Thermal Effusivity $[Ws^{1/2}m^{-2}K^{-1}]$	1289.3	1627.4
South ROI Thermal Effusivity $[Ws^{1/2}m^{-2}K^{-1}]$	1217.8	1708.5
Sand ROI Thermal Effusivity $[Ws^{1/2}m^{-2}K^{-1}]$	1208.4	1920.2

The thermal diffusivities from the remote method have the same order of magnitude as the thermal diffusivites from the in situ methods. However, there is inherent error since night and morning values of the same ROI are different. Also, every in situ method resulted in a smaller thermal diffusivity for the southern profile compared to the northern. The remote method during the night had the opposite trend even though the night measurements were more temporally stable. The results of this study show promise for the remote methodology although further investigation is needed.

5.5   Future Work

For the Wolf River experiment there remains improvements and additions to the analysis that can be made. Collected core samples can be used to experimentally determine the thermal conductivity, thermal diffusivity, and moisture

content that can be compared with the various modeling approaches described in this chapter. Furthermore commercial models such as HYDRUS, can be used to model thermal diffusion using a 2D domain and additional surface boundary conditions.

Chapter 6

CONCLUSION

The methodology presented in this thesis allows for the quantitative transformation of temperatures from angular GBRS TIR imagery to the nadir equivalent temperatures. The method was first validated for a flat water surface and later applied to a flat, dry sand surface. The next steps would be to repeat the experiments at different temperatures, at different moisture contents, and for new materials. With more experimental data false temperature variability associated with oblique imagery may be fully accounted for.

Through the use of accurate GBRS TIR imagery we have demonstrated that thermal diffusivity can be acquired. This was validated by results from analyzing the in situ measurements. The next step, again, is to repeat this method with different moisture contents and different materials.

This study has developed a technique for determining physical properties of real world materials through oblique GBRS TIR imagery. Through use of the remotely determined thermal diffusivity it may even be feasible to infer other geotechnical properties.

REFERENCES

Balick, L. and B. Hutchinson (1986). "Directional thermal infrared exitance distributions from a leafless deciduous forest." *IEEE Transactions on Geoscience and Remote Sensing*, vol.GE-24, pp.693-698

Bertie, J.E., and Z. Lan (1996). "Infrared intensities of liquids XX: the intensity of the OH stretching band of liquid water revisited, and the best current values of the optical constants of H20(l) at 25°C between 15,000 and 1cm-1." *Applied Spectroscopy*, vol.50, no.8, pp.1047-1057

Carslaw, H.S. Introduction to the Mathematical Theory of the Conduction of Heat in Solids (Macmillan, edn. 2, 1921)

Carslaw, H.S., and J.C. Jaeger. Conduction of heat in solids. (Oxford, edn. 2, 1959).

Cuenca J., & J. A. Sobrino (2004). "Experimental measurements for studying angular and spectral variation of thermal infrared emissivity." *Applied Optics*, vol. 43, no. 23, pp. 4598-4602

Cuenca J., J. A. Sobrino, G. Soria (2005). "An experimental study of angular variations of brightness surface temperature for some natural surfaces." *Proceedings of the MERIS (A)ATSR Workshop 2005 (ESA SP-597)*. 26 - 30 September 2005 ESRIN, Frascati, Italy. Editor: H. Lacoste. Published on CDROM., p.33.1

Dozier, J. and S.G. Warren (1982). "Effect of viewing angle on the infrared brightness temperature of snow." *Water Resources Res.*, vol.18, no.5, pp.1424-1434

Fuchs, M. and C.B. Tanner (1968). "Surface temperature measurements of bare soils." *Journal of Applied Meteorology.*, vol.7, pp.303-305

Hale, G.M. and M.R. Querry (1973). "Optical constants of water in the 200-nm to 200μm wavelength region." *Applied Optics*, vol.12, no.3, pp.555-563

Hall, Jr., F.F. (1964). "The polarized emissivity of water in the infrared." *Applied Optics*, vol.3, no.6, pp.781-782

Hulley, G.C., S.J. Hook, and A.M. Baldridge (2010). "Investigating the effects of soil moisture on thermal infrared land surface temperature and emissivity using satellite retrievals and laboratory measurements." *Remote Sensing of Environment*, vol.114, pp.1480-1493

Ishida, T., A. Ando, and M. Fukuhara (1991). "Estimation of complex refractive index of soil particles and its dependence on soil chemical properties." *Remote Sensing of Environment*, vol.38, pp.173-182

Joeseph, J.H., W.J. Wiscombe, and J.A. Weinman (1976). "The delta-eddington approximation for radiative flux transfer." *J. Atmos. Sci*, vol.33, pp.2452-2459

Kimes, D.S., J.A. Smith, and L.E. Link (1981). "Thermal IR exitance model of a plant canopy." *Applied Optics*, vol.20, no.4, pp.623-632

Kirbus, A., I. Vishnevetsky, I, E. Rotenberg, and D. Yakir (2003). "Systematic errors in the measurements of emissivity caused by directional effects," *Applied. Optics*, vol.42, pp.1839-1846

Kruse, P.W., L.D. McGlauchlin, and R.B. McQuistan. Elements of Infrared Technology: generation, transmission, and detection (John Wiley & Sons, Inc., 1962)

Labed, J. and M. P. Stoll (1991). "Angular variation of land surface spectral emissivity in thermal infrared: laboratory investigations on bare soils", *International Journal of Remote Sensing*, vol.12, no.11, pp.2299-2310

Lagouarde, J.P., Y.H. Kerr, and Y. Brunet (1995). "An experimental study of angular effects on surface temperature for various plant canopies and bare soils." *Agricultural and Forest Meteorology*, vol.77, pp.167-190

Li, X., A.H. Strahler, and M.A. Friedl (1999). "A conceptual model for effective directional emissivity from nonisothermal surfaces." *IEEE Transactions on Geoscience and Remote Sensing*, vol.37, no.5, pp.2508-2517

Masuda, K., T. Takashima, and Y. Takayama (1988). "Emissivity of pure and sea waters for the model sea surface in the infrared window regions." *Remote Sensing of Environment*, vol.42, pp.1060-1071

McAtee, B. K., A. J. Prata, and M. J. Lynch (2003). "The angular behavior of emitted thermal infrared radiation (8– 12 mm) at a semiarid site." *Journal of Applied Meteorology*, vol.42, pp.1060-1071

Minacapilli M., M. Iovino, and F. Blanda (2009). "High resolution remote estimation of soil surface water content by a thermal inertia approach." *Journal of hydrology*, vol.379, no.3-4, pp.229-238

Mira, M., E. Valor, R. Boluda, V. Caselles, and C. Coll (2007). "Influence of soil water content on the thermal infrared emissivity of bare soils. Implication for land surface temperature measurement." *Journal of Geophysical Research*, 112, F04003

Modest, M.F. Radiative Heat Transfer (Academic Press, edn. 2, 2003)

Niclos, R., E. Valor, V. Caselles, C. Coll, and J.M. Sanchez (2005). "In situ angular measurements of thermal infrared sea surface emissivity-validation of models." *Remote Sensing of Environment*, vol.94, pp.83–93

Ninomiya Y., F. Bihong, and T. J. Cudahy (2005). "Detecting lithology with Advanced Spaceborne Thermal Emission and Reflection Radiometer(ASTER) multispectral thermal infrared 'radiance-at-sensor' data." *Remote Sensing of Environment*, vol.99, no.1/2, pp.127–139

Oren, M. and S.K. Nayar (1995). "Generalization of the Lambertian Model and Implications for Machine Vision." *International Journal of Computer Vision*, vol.14, no.3, pp.227-251

Qin, Z. and A. Karnieli (1999). "Progress in the remote sensing of land surface temperature and ground emissivity using NOAA-AVHRR data." *International Journal of Remote Sensing*, vol.20, no.20, pp.2367–2393

Querry, M.R., W.E. Holland, R.C. Waring, L.M. Earls, and M.D. Querry (1997) "Relative reflectance and complex refractive index in the infrared for saline environmental waters." *Journal of Geophysical Research*, vol.82, no.9, pp.1425-1433

Rees, W.G., and S.P. James (1992) "Angular variation of the infrared emissivity of ice and water surfaces." *International Journal of Remote Sensing*, vol.13, no.15, pp.2873-2886

Richter, N.B. (1962). "The photometric properties of interplanetary matter." *Quart. J. Roy. Astronom. Soc*, vol.3, pp.179-186

Sidran, M. (1981). "Broadband reflectance and emissivity of specular and rough water surfaces." *Applied Optics*, vol.20, no.18, pp.3176-3183

Spitzer, W.G. and D.A. Kleinman (1961). "Infrared Lattice Bands of Quartz." *Physical Review*, vol.121, no.5, pp.1324-1335

Snyder, W. C., Z. Wan, Y. Zhang, and Y.Z. Feng (1997). "Thermal infrared (3-14 μm) bidirectional reflectance measurements of sands and soils." *Remote Sensing of Environment*, vol.60, pp.101-109

Snyder, W. C., Z. Wan, and X. Li (1998). "Thermodynamic constraints on reflectance reciprocity and Kirchhoff's law" *Applied Optics*, vol.37, no.16, pp.3464-3470

Sobrino, J.A., and J. Cuenca (1999). "Angular variation of thermal infrared emissivity for some natural surfaces from experimental measurements." *Applied Optics*, vol.38, no.18, pp.3931-3936

Takashima, T., and Y. Takayama (1981). "Emissivity and reflectance of the model sea surface for the use of AVHRR data of NOAA satellites." *Papers in Meteorology and Geophysics*, vol.32, no.4, pp.267-274

Vitkovskii, V.V., V.G. Gorshenev, and Yu.F. Potapov (2009). "Measurement of spectral directional emissivity of materials and coatings in the infrared region of spectrum." *Thermal Engineering*, vol.56, no.3, pp.245-248

Watts, P.D., M.R. Allen, and T.J. Nightingale (1996). "Wind speed effects on sea surface emission and reflection for the along track scanning radiometer." *Journal of the Atmospheric and Oceanic Technology*, vol.13, pp.126-141

Wiscombe, J., and S.G. Warren (1980). "A model for the spectral albedo of snow. I: Pure Snow." *Journal of the Atmospheric Sciences*, vol.37, pp.2712-2733

Wu, X., and W.L. Smith (1997). "Emissivity of rough sea surface for 8-13μm: modeling and verification." *Applied Optics*, vol.36, no.12, pp.2609-2619

Appendix I

VARIABLE LIST

A	Amplitude $[K]$
cp	Specific heat capacity $[J kg^{-1} K^{-1}]$
$d\Omega$	Infinitesimal Solid Angle $[sr]$
f(z)	Initial temperature profile through depth $[K]$
F_0	Constant heat flow density $[W m^{-2}]$
FOV	Angle that describes the Field Of View of our imager in the axis of interest. The imager has a FOV for the x-direction and a FOV for the y-direction. $[°]$
H_p	Height from pivot to surface $[m]$
IFOV	Angle that describes both the Field of View of a single pixel in our imager (independent of axis) and the angle between the rays projected from the center of two neighboring pixels to the focal point. $[°]$
k	Thermal conductivity $[W m^{-1} K^{-1}]$
L_E	Length of Extra distance due to having goniometer pivot above the target surface $[m]$
L_F	Length of Focal Distance $[m]$
L_G	Length of Goniometer Arm $[m]$
L_{rp0}	Length of the ray projected from bottom boundary of bottom pixel $[m]$
L_{rp1}	Length of the ray projected from the first pixel $[m]$
L_{rpj}	Length of the ray projected from the center of the j'th pixel $[m]$
L_T	Length of distance from imager to target $[m]$
LFOV	Length of the projection of the FOV on the Target Surface $[m]$
M_E	Radiance emitted by surface $[W m^{-2} sr^{-1}]$
$M_E(T)$	Total emitted radiance into a hemisphere by a surface $[W m^{-2} sr^{-1}]$
$M_{E,bb}(T)$	Total emitted radiance into a hemisphere by a black body $[W m^{-2} sr^{-1}]$
$M_{E,\lambda}(T)$	Emitted radiance into a hemisphere by a surface for a given spectral interval $[W m^{-2} sr^{-1}]$
$M_{E,bb,\lambda}(T)$	Emitted radiance into a hemisphere by a black body for a given spectral interval $[W m^{-2} sr^{-1}]$
$M_{E,\omega,\lambda}(T)$	Emitted radiance into a given solid angle by a surface for a given spectral interval $[W m^{-2} sr^{-1}]$
$M_{E,bb,\omega,\lambda}(T)$	Emitted radiance into a given solid angle by a black body for a given spectral interval $[W m^{-2} sr^{-1}]$
$M_{E,\theta}$	Radiance emitted by surface at angle θ $[W m^{-2} sr^{-1}]$
$M_{IM,\theta}$	Radiance used by imager to determine T_θ $[W m^{-2} sr^{-1}]$

M_P	Radiance reflected by surface $[Wm^{-2}sr^{-1}]$
$M_{P,N}$	Radiance reflected off the surface at nadir $[Wm^{-2}sr^{-1}]$
$M_{P,\theta}$	Radiance reflected off the surface at angle θ $[Wm^{-2}sr^{-1}]$
M_{tot}	Total radiance observed by imager $[Wm^{-2}sr^{-1}]$
$M_{tot,\theta}$	Total radiance observed by imager at angle θ $[Wm^{-2}sr^{-1}]$
M_{TR}	Radiance lost to transmitting medium $[Wm^{-2}sr^{-1}]$
n	Complex index of refraction [*unitless*]
p	Reflectivity [*unitless*]
p_λ	Spectral reflectivity [*unitless*]
$p_{\omega\lambda}^{\cap}(T,\hat{S})$	Spectral directional-hemispherical reflectivity [*unitless*]
p_θ	Angular reflectivity, simplified notation of spectral directional-hemispherical reflectivity for a given spectrum and temperature when observed at angle θ [*unitless*]
$p_\parallel$	Parallel polarized reflectivity [*unitless*]
$p_\perp$	Perpendicular polarized reflectivity [*unitless*]
q	Imaginary part of a material's index of refraction [*unitless*]
$\hat{S}$	Direction vector, composed of a polar angle (θ) and an azimuth angle (φ) [°,°]
$\hat{S}_i$	Incident light radiation [°,°]
$\hat{S}_r$	Reflected radiation [°,°]
$\hat{S}_t$	Transmitted radiation [°,°]
t	Time [*sec*]
T	Temperature [*K*]
T_0	Amplitude (temperature) [*K*]
T_m	Datum temperature [*K*]
T_o	Object temperature [*K*]
T_P	Reflected temperature [*K*]
T_θ	Temperature observed at angle θ [*K*]
T_θ^M	Measured angular temperature [*K*]
T_θ^P	Predicted angular temperature [*K*]
z	Depth [*m*]
z'	Variable of integration
ά	Thermal diffusivity $[m^2/sec]$
α	Absorptivity [*unitless*]
α_λ	Spectral absorptivity [*unitless*]
$\alpha_{\omega\lambda}(T,\hat{S})$	Spectral directional absorptivity [*unitless*]
δ	Period [*sec*]
ε	Phase [*rad*]
ε	Emissivity [*unitless*]
$\varepsilon_{eff}(T)$	Effective hemispherical emissivity [*unitless*]
$\varepsilon_{\lambda hem}(T)$	Spectral hemispherical emissivity [*unitless*]

$\varepsilon_{\omega\lambda}(T, \hat{S})$	Spectral directional emissivity [*unitless*]
ε_N	Nadir emissivity, simplified notation of spectral directional emissivity for a given spectrum and temperature when observed at nadir [*unitless*]
ε_θ	Angular emissivity, simplified notation of spectral directional emissivity for a given spectrum and temperature when observed at angle θ [*unitless*]
ζ	Porosity [*%*]
η	Real part of a material's index of refraction [*unitless*]
θ	Polar angle (from nadir) used for describing emission angle and imager observation angle [°]
θ_1	Incident angle [°]
θ_2	Angle of transmission [°]
θ_{B0}	Angle bounded by target surface and the ray projected from the imagers FOV boundary [°]
θ_{B1}	Angle bounded by target surface and the ray projected from center of the first pixel in the imager [°]
θ_{Bj}	Angle bounded by target surface and the ray projected from the center of the j'th pixel [°]
θ_{ij}	Incident angle for a particular pixel [°]
θ_R	Incident angle for a pixel [°]
ρ	Density [kg/m^3]
σ	Stefan-Boltzmann constant, 5.67e-8 $Js^{-1}m^{-2}K^{-4}$
τ	Variable of integration
τ_λ	Spectral transmissivity [*unitless*]
ϕ	Azimuth angle [°]
$\phi(t)$	Surface temperature profile through time [*K*]
$\acute{\omega}$	Angular Frequency [rad/sec]

General Subscripts/Superscripts

0	Initial, at surface
E	Emissive
i	Some number
I	Incident upon surface
j	Some number
n	Some number
N	Nadir
o	Object or material specific
P	Reflective
θ	Angular
λ	Spectral, electro-magnetic spectrum
ω	Solid angle

Appendix II

CALIBRATIONS

Table II.1: Calibrations for Kinetic Sensors (Dynamax TM10 Temperature Probes)

Sensor #	Slope	Intercept	R^2
1	1.0049	-0.074	0.9999
2	1.0118	-0.0616	0.9997
3	0.9983	0.1662	0.9999
4	0.9965	0.2365	0.9999
5	0.9963	0.2352	0.9999
6	0.9987	0.1455	0.9999
7	0.9961	-0.0984	0.9999
8	0.9966	-0.0735	0.9999
9	0.9981	0.0076	0.9999
10	0.9906	0.2828	0.9999
11	1.003	0.1271	0.9999
12	0.996	0.0423	0.9999
13	0.9972	0.0832	0.9999
14	0.9953	0.0385	0.9999
15	0.9935	0.1642	0.9999
16	0.9943	-0.0807	0.9999
17	0.9949	0.196	0.9999
18	0.995	0.091	0.9999
19	0.9955	0.1322	0.9999
20	0.9972	0.0783	0.9999
21	0.9974	0.0251	0.9999
22	0.9908	0.0171	0.9999
23	0.9986	0.121	0.9999
24	0.9983	0.1881	0.9999

Table II.2: Calibrations for Omega Type K Thermocouples

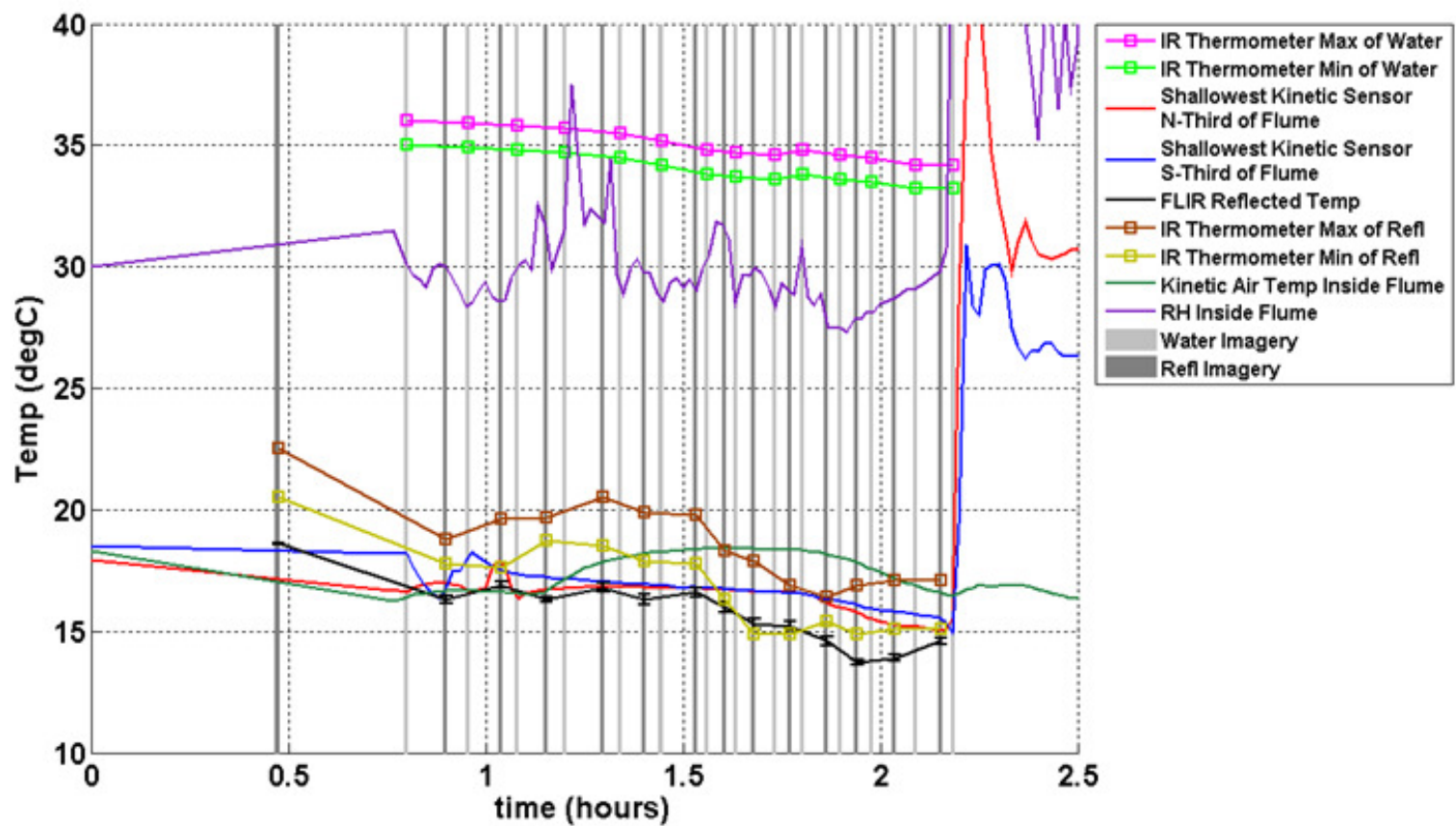| Sensor #	Slope	Intercept	R^2
1	1.0121	-3.5269	0.9999
2	1.0118	-2.9762	0.9998

Appendix III

EXPERIMENTAL MEASURED DATA

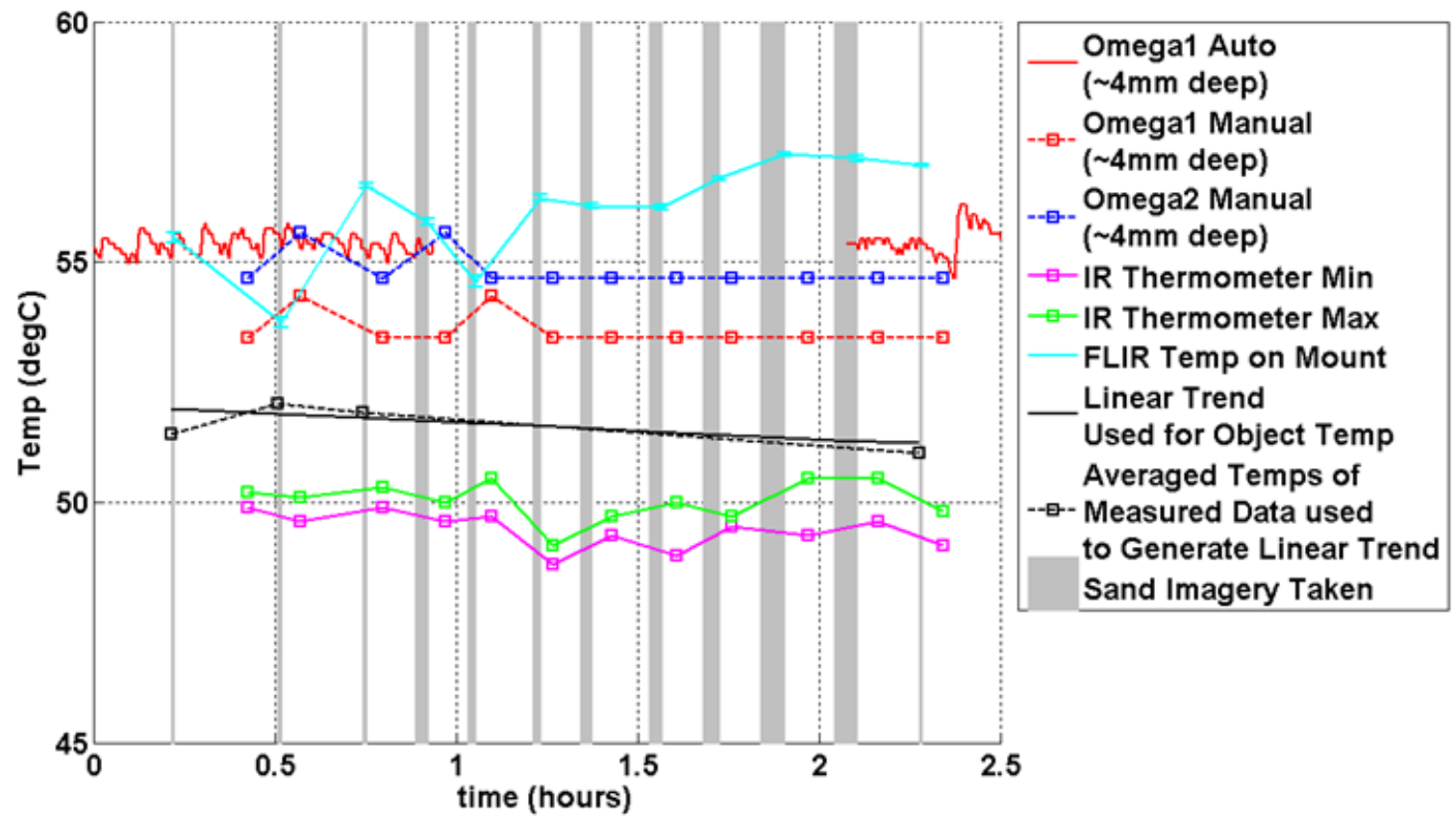**Figure III.1: Water Experiment Measured Data**
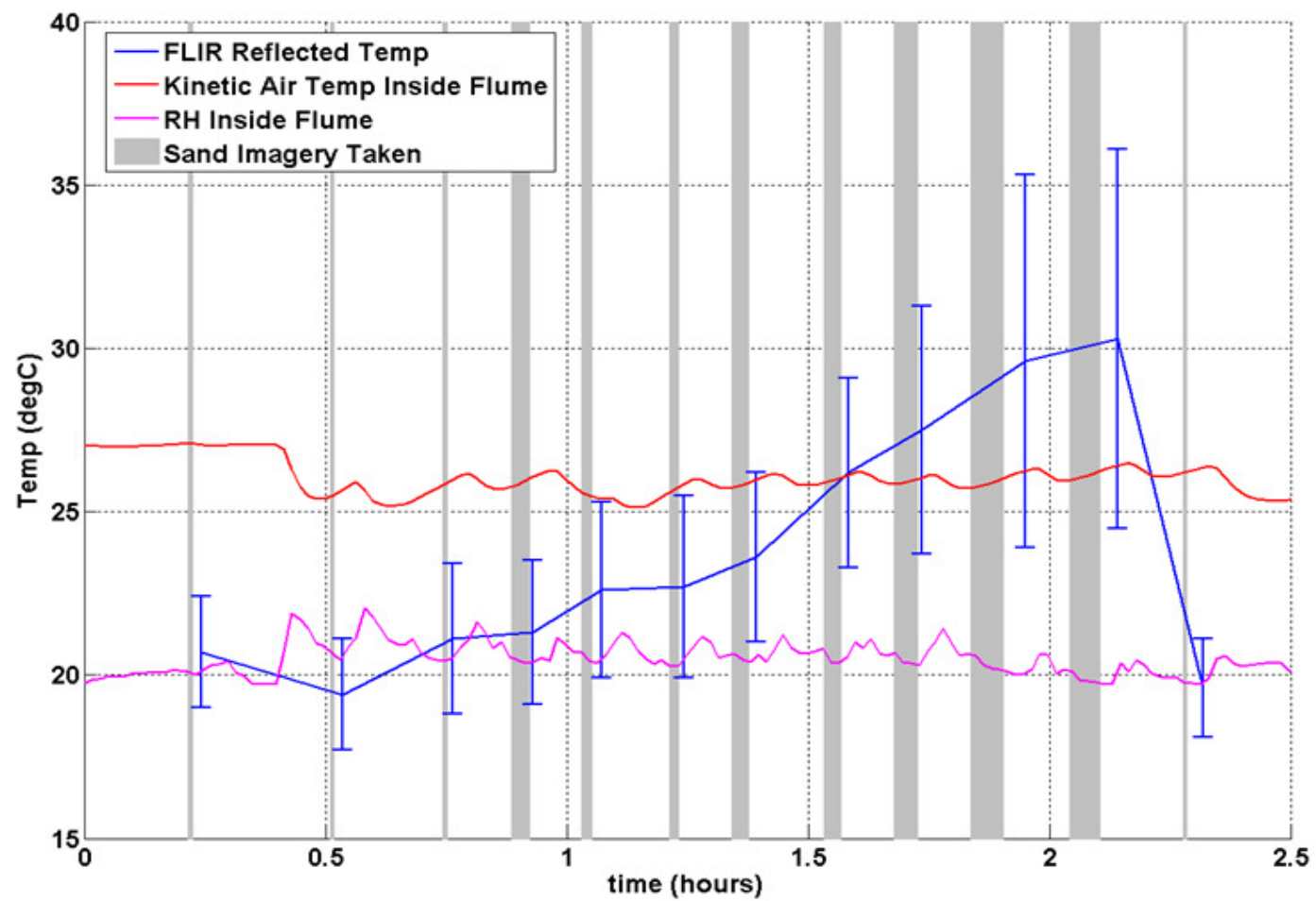
Figure III.2: Sand Experiment Measured Data

Figure III.3: Sand Experiment Measured Data Continued